Applied Thermal Engineering 159 (2019) 113980

Contents lists available at ScienceDirect

Applied Thermal Engineering

journal homepage: www.elsevier.com/locate/apthermeng

Research Paper

Numerical study on latent thermal energy storage systems with aluminum foam in local thermal equilibrium

Bernardo Buonomo[a], Hasan Celik[b], Davide Ercole[a], Oronzio Manca[a,*], Moghtada Mobedi[c]

[a] Dipartimento di Ingegneria, Università degli Studi della Campania "Luigi Vanvitelli", via Roma 29, 81031 Aversa, CE, Italy
[b] Department of Mechanical Engineering, Izmir Institute of Technology, Urla, Izmir 35430, Turkey
[c] Faculty of Engineering Shizuoka University 3-5-1 Johoku, Hamamatsu, Japan

HIGHLIGHTS

- Analyses of Latent Heat Thermal Energy Storage Systems based on a Phase Change Material.
- Enthalpy-porosity model to describe the melting of the PCM in metal foams.
- The metal foam is modelled by Darcy-Forchheimer law and in local thermal equilibrium.
- Comparisons are made between clean cases and porous cases for the different porosities.
- Results show that the presence of metal foam improves the overall heat transfer rate.

ARTICLE INFO

Keywords:
Thermal energy storage
Phase change materials
Porous media
Metal foams
Numerical investigation

ABSTRACT

The paper analyzes the behavior of a Latent Heat Thermal Energy Storage system (LHTES) with a Phase Change Material (PCM), with and without aluminum foam. A numerical investigation in a two-dimensional domain is accomplished to investigate on the system thermal evolution. The enthalpy-porosity method is used to describe the PCM melting. The open-celled aluminum foam is described as a porous medium by means of the Darcy-Forchheimer law. A hollow cylinder represents the considered thermal energy storage and it consists of the enclosure between two concentric shell tubes. The external surface of the internal tube is at assigned temperature with a value greater than the melting PCM temperature, while the other surfaces are adiabatic. Local thermal equilibrium (LTE) is numerically adopted for modelling the heat transfer between the PCM and the solid matrix in aluminum foam. In the case with metal foam, simulations for different porosities are performed. A comparison in term of liquid fraction, average temperature of the system, temperature fields, stream function and a performance parameter are made between the clean case and porous assisted case for the different porosities. A scale analysis is developed for evaluating the time and the melting zone in different regimes (i.e. conduction, mixed conduction-convective and convective) during the melting processes of the PCM in porous media. Numerical simulation shows that aluminum foam increases overall heat transfer by a magnitude of two, with respect to the clean case.

1. Introduction

The environmental problems, the high cost of energy and the continuous and growing energy demand are important issues occupying a wide part of the scientific research. The main problem is to avoid wasting excess energy therefore it is important to design, construct and use a buffering system to reduce the gap between the supply and the energy demand. A Latent Heat Thermal Energy Storage System (LHTESS) can operate like a buffer system [1] since it stores thermal energy in surplus and then releases energy when it is required. For example, the installation of a LHTESS in a thermal solar plant has an important advantage because it can fill up the temporary absence of the energy supply, for example in the cloudy days. The latent heat thermal energy storage system (LHTESS) is based on the phase change materials (PCMs) [2,3] where the phase-change process can be utilized to absorb and release thermal energy related to high latent heat value of the

* Corresponding author at: Dipartimento di Ingegneria, Università degli Studi della Campania "Luigi Vanvitelli", Real Casa dell'Annunziata, Via Roma 29, 81031 Aversa, CE, Italy.
E-mail addresses: bernardo.buonomo@unicampania.it (B. Buonomo), davide.ercole@unicampania.it (D. Ercole), oronzio.manca@unicampania.it (O. Manca), moghtada.mobedi@shizuoka.ac.jp (M. Mobedi).

https://doi.org/10.1016/j.applthermaleng.2019.113980
Received 1 July 2018; Received in revised form 11 June 2019; Accepted 16 June 2019
Available online 18 June 2019
1359-4311/

Nomenclature

A_{mush}	mushy zone costant [kg m^{-3}s^{-1}]
c	specific heat [J kg^{-1} K^{-1}]
C_F	inertial drag factor
D	length of diffusion region [m]
d_f	ligament diameter [m]
d_p	pore diameter [m]
E	specific enthalpy [J kg^{-1}]
Fo	Fourier number
g	gravity acceleration [m s^{-2}]
H	height of LHTES [m]
H_L	latent heat of PCM [J kg^{-1}]
k	thermal conductivity [W m^{-1} K^{-1}]
K	permeability [m^2]
L	characteristic length [m]
p	pressure [Pa]
q	performance parameter [Eq. (14)]
Ra	Rayleigh number
r	radial cylindrical coordinate [m]
r_i	internal radius of LHTES [m]
r_e	external radius of LHTES [m]
S	source term [Eqs. (5)–(6)]
t_c	initial time of convection [t]
t	time [s]
T	temperature [K]
T*	non-dimensional temperature
$T_{solidus}$	solidus temperature [K]
$T_{liquidus}$	liquidus temperature [K]
T_{wall}	wall temperature [K]
u	r-component velocity [m s^{-1}]
w	z-component velocity [m s^{-1}]
z	axial coordinate [m]
z_L	vertical thickness [m]

Greek Symbols

α	Thermal diffusivity [m^2 s^{-1}]
β	liquid fraction [Eq. (1)]
δ	layer of thickness [m]
γ	thermal expansion coefficient [K^{-1}]
ε	porosity
μ	viscosity of PCM [kg m^{-1} s^{-1}]
ρ	density [kg m^{-3}]
ω	pore size [Pore per Inch (PPI)]

subscripts

0	operating
eff	effective
i	initial
m	melting
mf	metal foam
p	phase change material
r	radial
Δt	time step
W	wall
Z	axial

material. The PCMs are widely utilized for thermal storage system due to their capability of storing energy with a nearly constant temperature and for their high energy stored density values, as reported in various books related to thermal energy storage system [4,5], power generation and heat supply [6], sustainable energy [7,8] or reported in various reviews for different applications such as electricity generation and road transportation [9], demand-side management [10], solar plants [11], HVAC systems [12], building [13], solar cooling [14], heat pump [15], desalination processes [16] and data center thermal management [17].

There are mainly three types of PCMs: organic [18], inorganic [19,20] and eutectic. A good compromise is found in the organic PCM; in paraffin wax, because it presents a high latent heat, it is non-toxic, non-expensive [52] in respect to the other PCMs and chemically stable and abundant in nature [21]. However, the main weakness is the low thermal conductivity value and this leads the whole thermal storage system to be ineffective, from an engineering standpoint, because of the long and not-controlled time for melting. Such problem can be overcome with different enhancement techniques [22] such as metal foam [23], micro-capsulation [24], carbon-fiber brushes [25], expanded natural graphite (CENG) matrix [26]. In particular, the use of the metal foams seems to be a good solution to improve the thermal conductivity of the whole system. A comparative work between two enhancement technique was accomplished by Chow et al. [27]. The first enhancement technique employs PCM encapsulated in smaller tanks of different geometrical configurations. The second enhancement technique is based on metal foam. By the results, it seems that the metal foam was the best enhancement technique in terms of thermal conductivity.

Zhao et al. [28] experimentally examined the organic paraffin wax, inorganic hydrate salts and inorganic sodium nitrate with metal foams and expanded graphite. Their results showed that the metal foam provides better heat transfer performance but reducing the buoyancy effect of the liquid PCM.

Tian et al. [29] numerically studied the natural convection effects on heat transfer behavior for PCM in presence of metal foam. Two cases are investigated, one with metal foam and the other without metal foam. By the results, the presence of metal foam suppresses the natural convection of PCM in the liquid phase, nevertheless the overall heat transfer performance is improved.

An experimental investigation was accomplished by Zhao et al. [30], where the PCM in metal foam is heated for charging process and then it is cooled for discharging process. The metal foam is a copper foam and the PCM is the RT58 paraffin wax, employed for low-temperature storage application. By the results the presence of metal foam is very significant because the heat transfer rate could be augmented between 5 and 20 times. The numerical investigation of a similar work with the same material was accomplished in [31], where it is showed that the metal foam increases the melting time.

An experimental and numerical investigation was carried out by Siahpush et al. [32] to determine the heat transfer enhancement in a thermal energy storage system in cylindrical geometry employing copper foam in local thermal equilibrium (LTE) assumption. Zhou et al. [33] experimentally investigated the heat transfer performance of PCM embedded in open-cell metal foams and expanded graphite. The results showed that the overall heat transfer rate improves especially with metal foam. A comparison between experimental and numerical study on PCM melting in metal foam was performed by Chen et al. [34] using the Lattice Boltzmann method. A numerical investigation to study an LTESS embedded with heat pipes and PCM in metal foam for concentrating solar power system was accomplished by Nithyanandam and Pitchumani [35]. Enthalpy porosity method was employed in numerical model for both charging and discharging phases of the system. Simulations at varying the parameters of metal foam and arrangements of heat pipes were performed. A three-dimensional model to study an LHTESS embedded with PCM in metal foam and with fins was presented by Sundarram and Li [36]. LTE model was assumed, and term was added in the momentum equation to take into account the Darcy-Forchheimer law and natural convection in the liquid part of the PCM.

A shell-and-tube LHTESS was investigated by Liu et al. [37]. The melting process of the PCM in aluminum foam was numerically analyzed to evaluate the porosity and pore size of the foam effects on thermal performances. Tao et al. [38] numerically investigated a system with PCM in metal foam for different porosity and pores per inch (PPI). An optimum structure of metal foam with porosity and pore density equal to 0.94 and 45, respectively, was achieved in terms of the following storage behaviors: heat capacity, density and PCM melting rate. A numerical and experimental investigation on heat transfer characteristics of the PCM embedded in a metal foam was reported by Zhang et al. [39]. Local Thermal Non-Equilibrium (LTNE) assumption was used to model the thermal behavior of the PCM in metal foam. The comparison between experimental measurements and numerical simulations was acceptable. Yang et al. [40] presented a transient mathematical model to study the influence of the porosity variation on the thermal behavior of a system based on PCM, numerically. The results indicate that with the varying porosity, there is a beneficial effect on the melting rate. A shell-tube arrangement of a Latent Heat Thermal energy system with PCM embedded in metal foam is carried out by Atal et al. [41] in experimental and numerical ways for different porosities (95% and 77%). The results show that, the lower-porosity foam has a faster charging and discharging time cycle in relation to the higher-porosity foam, and this is a consequence of higher overall thermal conductivity associated with the lower porosity foam. Moreover, the experimental results are in agreement with the numerical simulations. A numerical study on PCM with porous matrix for a cylindrical configuration in horizontal configuration is accomplished in Mesalhi et al. [42], where they stated that the presence of the porous matrix increases the melting rate of the PCM, especially for lower porosity. Kumar et al. [43] have accomplished an exergy and energy analyses of shell and tube type latent heat thermal storage systems (LHTES) for solar thermal power plant for charging and discharging cycles. The system is improved applying a metal matrix and by the results at low porosity the system is more efficient, in particular the entropy generation is minimal for porosity set to 0.85. A similar study was accomplished in [44] with a variable porosity function and by the results it is possible to reduce the storage volume with variable porosity of the porous media obtaining the same performance. A shell-and-tube latent heat thermal storage system was experimentally investigated using paraffin wax as PCM in Yang et al. [45]. A differential scanning Calorimetry was employed to characterize the thermal properties of the PCM, such as latent heat and melting temperature range. Copper foam is employed to improve the properties of the system. Different heating temperatures and flow rates are investigated. By the results, the temperature distributions in the system have shown a more uniform distribution with metal foam than with the pure paraffin. Moreover, the melting time is shorter by one third of the pure paraffin system with the same operating conditions. Wang et al. [46] have accomplished an experimental test system with paraffin and metal foam on a uniform temperature heating platform. A comparison with numerical results is also made and the temperature values calculated by the numerical model are in agreement to the temperature measurements carried out for the second stage of the melting process, but the first stage presents a deviation. This could be explained by the copper foam oxidation and by the non-uniform paraffin melting. Huang et al. [47] have characterized a Myristyl alcohol (PCM) with metal foam to determine the thermal properties of PCM/metal foam during solidification and melting changing phases. They analyzed the chemical structure using a Fourier transformation infrared spectroscope (FT-IR), the X-ray diffractometer for the crystalloid structure, a Scanning Electron Microscope for the morphologies and a thermogravimetry for the thermal stability. It was found that: no chemical interaction takes place between PCM and metal foam, there is a slight decrease of the latent heat, a slight increase of melting temperature when the metal foam is present, with steady stability. Melting process of paraffin on metal foam has been numerically investigated in a 3D model by Zhang et al. [48], using two types of structures of metal foam skeletons, body-centered cubic BCC and face-centered cubic FCC in order to visualize the velocity field at pore scale. An experimental setup has been also set to validate the model. The results show that BCC and FCC structures shorten the melting time by 26% and 28%, respectively. A numerical analysis of a 2D box with PCM and metal foam has been investigated by Zhu et al. [49]. The improvement technique consists adding fins and metal foam with graded porosity. A Local Thermal Non Equilibrium assumption is considered. By the results, it seems that the gradient porosity has a small effect on melting rate. A three-dimensional numerical model has been investigated in Zhang and He [50] with two types of metal foam with a gradient porosity. Heat flux at the left side of the box was induced, while the other surfaces are adiabatic. Results show that, the heat conduction phenomenon plays a key role in the heat transfer processes; the metal foam with gradient porosity has the major heat storage rate compared to the constant porosity foam. A paraffin/copper foam composite PCM in a rectangular enclosure made of Plexiglas has been numerically and experimentally investigated in Zhang et al. [51] The mathematical model includes the enthalpy-porosity method and the Local Thermal Non-Equilibrium assumption is employed. By the results, there is a reasonable agreement between numerical model and experimental setup. The effect of the height ratio between the copper foam and the heat sink with PCM has been studied in Zhu et al. [52] The height of copper foam varies between 0 (no metal foam) and 20 mm (the height of the heat sink). The bottom surface is heated and the other surfaces are thermally insulated. The results showed that higher height ratios improve the thermal performance of the heat sink but increase the weight and the costs of the whole system. Yang et al. [53] studied numerically an LHTES device with a composite structure employing both fins and copper foam. It was found that the combined use reduced the charging and the discharging times significantly. One of the first investigation on PCM in metal foam to enhance the effective thermal conductivity was accomplished by Krishnan et al. [54]. They underlined that the PCM in metal foam can determine a less overheating though at steady state the system has a lower melt volume fraction. More recently, the charge and discharge phases of an LHTES was studied by Buonomo et al. [55] for a shall a tube geometry and the analysis was provided considering an LTNE model. A parallelepiped TES with internal tubes and nano-PCM in aluminum foam was numerically investigated by Buonomo et al. [56]. It was found that the presence of Al_2O_3nanoparticles did not improved the thermal behaviors of the LHTES for the examined volumetric concentration.

In Table 1, the reviewed papers are summarized, and it is observed that there is a lack of numerical investigations on LHTES systems with metal foam embedded in PCM for a cylindrical geometry. The present configuration has various applications as latent thermal storage mainly in solar energy systems at different operation temperatures from low ones to high ones, as given in [3,32,37,41,57]. This convinced the authors to examine the phenomenological aspects of this configuration related to the low operation temperature solar energy systems developing a scale analysis.

In the present investigation, an LHTES system is numerically studied. Specifically, the study is focused on a vertical hollow cylinder filled up with PCM and an assigned temperature on the surface of the internal cylinder and assuming that the heat transfer towards the external ambient is negligible. A scale analysis is developed to estimate the main parameters in the different regimes/regions during the melting processes of the PCM in porous medium. Simulations for different porosity values, at assigned pores per inch (PPI) equals to 20, are carried out. The results are shown in terms of melting time, average temperature of the system, and a performance parameter.

2. Geometrical and physical models

The LHTES system and its geometrical configuration, a hollow cylinder under investigation are shown in Fig. 1. The cylindrical domain is

Table 1
Summary of open literature for Latent Heat Thermal Energy Storage with PCM.

Ref. (year)	Exp/Num	Configuration system	PCM	PCM Latent Heat [kJ kg^{-1}]	Melting Mean Temperature [K]	PCM Thermal conductivity [W m^{-1} K^{-1}]	Method for phase change process	Improvement technique	Material of the improved material
[21] (2004)	Both	Cealing Panel with fin	-Hexadecane -Heptadecane -Octadecane	236 214 244	291 295 301	0.17–0.26	Stefan problem	fins	–
[27] (1996)	Num.	Cylindrical/shell	Lithium hydride (LiH)	258	958	4.2	finite-element method	-Encapsulation -Metal foam	Nickel
[28] (2010)	Exp	Box	-paraffin RT27 -hydrate calcium chloride -sodium nitrate	179 190.8 173.3	300 302 580	Solid: 0.24 Liquid: 0.15 Solid: 1.09 Liquid: 0.54 Solid: 0.50 Liquid:0.553	–	Metal foam expanded graphite	Copper Steel alloy Graphite
[31] (2009)	Both	Rectangular	Paraffin RT58	181	331	0.2	Moving melting interface	Metal foam (LTE)	Copper
[29] (2010)	Both	Rectangular	Paraffin RT58	181	331	0.2	Stefan problem	Metal foam (LTNE)	Copper
[30] (2010)	Both	Rectangular	Paraffin RT58	181	331	0.2	Enthalpy-porosity	Metal foam (LTNE)	Copper
[24] (2009)	Exp	Characterization work	n-Octacosane	86.4	323.6	–	–	Microencapsulation	polymethylmetracrylate (PMMA)
[25] (2003)	Both	heat exchanger	Paraffin wax	180	319.5	0.21 solid 0.12 liquid	apparent specific heat	Brushes	Carbon-Fiber
[26] (2001)	Exp	Cubic box	-Aldrich Paraffin wax -Fluka Paraffin wax -Hexadecane	– 	349.5 264 291.1	0.24	–	Expanded graphite powders	Graphite
[32] (2008)	Both	Cylindrical	eicosane	–	309.5	0.423	–	Metal foam (LTE)	Copper
[33] (2011)	Exp.	Rectangular	-Paraffin RT27 -calcium chloride hexahydrate (CaCl2-6H20)	184 109.8	298–301 302	0.24 solid 0.15 liquid 1.09 solid 0.54 liquid	–	Graphite powder Copper metal foam	Expanded graphite Copper
[34] (2014)	Both	Rectangular	Paraffin	120.	328–333	0.22	Lattice Boltzmann	Metal foam (LTE)	Aluminum
[35] (2014)	Num.	tube-in-shell	56% Li2CO3-44% Na2CO3	370	769.15	0.77	Enthalpy-porosity	Metal foam (LTNE)	–
[36] (2014)	Num.	Rectangular	Paraffin	180	321–335	0.2	Apparent specific heat (Heaviside)	Metal foam (no porous media formulation)	Aluminum
[37] (2013)	Num.	3D Cylindrical	Paraffin RT58	181	321–335	0.2	Enthalpy-porosity	Metal foam (LTNE)	Aluminum
[38] (2016)	Num.	Square	Paraffin	102.1	327	0.2	Lattice Boltzmann	Metal foam (LTNE)	Copper
[39] (2015)	Both	Rectangular plate	Paraffin	–	–	–	Enthalpy-porosity	Metal foam (LTNE)	Copper
[40] (2015)	Num.	Rectangular	sodium nitrate	178	579.15–580.15	0.51	Enthalpy-porosity	Metal foam (LTE)	Copper
[41] (2016)	Both	Shell-and-tube arrangement	Paraffin	117	328	0.25	Enthalpy-porosity	Metal foam (LTE)	Aluminum
[42] (2005)	Num	Shell-and-tube arrangement	Pr = 46.1	–	–	–	Stefan problem	Porous matrix (LTNE)	–
[43] (2016)	Num.	Shell-and-tube arrangement	Organic A164	249.7	441.8	0.425	Enthalpy-porosity	Metal foam (LTNE)	Stainless steel SS316
[44] (2018)	Num.	Shell-and-tube arrangement	Organic A164	249.7	441.8	0.425	Enthalpy-porosity	Metal foam (LTNE)	Stainless steel SS316
[45] (2016)	Exp	Rectangular box	Paraffin	136.4	322	0.3 solid 0.1 liquid	–	Metal foam	Copper
[46] (2016)	Both	Rectangular box	Paraffin	170.4	315.4	0.48–0.06 (from 298 K to 321 K)	Enthalpy-porosity	Metal foam (LTE)	Copper
[47] (2017)	Exp.	Characterization work	Myristyl alcohol	218.4	311.4	0.17	Enthalpy-porosity	Metal foam	Copper Nickel
[48] (2017)	Both	3D Box	Paraffin	200	325–330	0.558 solid 0.355 liquid	Apparent specific heat	Metal foam (Direct simulation)	Aluminum
[49] (2017)	Num	2D Box	Sodium Acetate	226	330–332	0.6	Enthalpy-porosity	Metal foam (LTNE)	Aluminum
[50] (2017)	Num.	3D box	Paraffin	200	325–330	0.588 solid 0.355 liquid	Apparent specific heat	Metal foam (LTE)	Aluminum

(*continued on next page*)

Table 1 (*continued*)

Ref. (year)	Exp/Num	Configuration system	PCM	PCM Latent Heat [kJ kg^{-1}]	Melting Mean Temperature [K]	PCM Thermal conductivity [W m^{-1} K^{-1}]	Method for phase change process	Improvement technique	Material of the improved material
[51] (2017)	Both	Rectangular Enclosure	Paraffin	175.24	327.6–337.3	0.3 solid 0.1 liquid	Enthalpy-porosity	Metal foam (LTNE)	Copper
[52] (2018)	Exp.	Rectangular Heat sink	Paraffin	121.	319	–	–	Partially Filled Metal Foam	Copper
57 [53] (2013)	Num.	Rectangular with fins	sodium nitrate	178	579.15–580.15	0.51	Enthalpy-porosity	Metal foam (LTE) and fins	Copper
59 [54] (2005)	Num.	2D non-dimensional Rectangular	–	–	–	–	Enthalpy-porosity	Metal foam (LTNE)	–
[55] 2017	Num.	Shell-and-tube arrangement	Paraffin	181	321–335	0.2	Enthalpy-porosity	Metal foam (LTNE)	Aluminum
[56] 2018	Num.	Tubes in parallelepiped	Nano-PCM (paraffin and Al_2O_3)	172	321–335	0.206	Enthalpy-porosity	Metal foam (LTNE)	Aluminum

given in Fig. 1a. The axial symmetry is assumed and the problem under investigation is two-dimensional, as shown in Fig. 1b. The system, with the height equal to H, is enclosed between an internal cylinder with a radius equals to r_i and an external cylinder with a radius equals to r_e, in Fig. 1b. H is 100 mm, r_i is 2 mm and r_e is 12 mm. The gravitational acceleration g, is directed along the z-axis and the phase change material (PCM) embedded in the aluminum foam are contained inside the two vertical cylinders. The boundary conditions are an assigned temperature, equals to 350 K, on the internal cylindrical surface, while the external surfaces are assumed adiabatic, as reported in Fig. 1c. The initial condition of temperature is 300 K.

The phase change material melts in a temperature range and the "enthalpy-porosity method" is adopted, to model the two phases of PCM melting and solidification, as given by Voller and Prakash [58]. In this method, during the melting process, there is no clear separation between the solid zone and the liquid zone but, a mixed solid-liquid zone is present. To describe the mixed region, a new parameter is defined, the liquid fraction, β. It expresses the ratio between the liquid volume and the total volume of a cell of the mixed region. It has a value between 0 and 1. The β value depends on the local temperature in the cell and in particular:

$$\begin{cases} \beta = 0 & \text{for } T < T_{solidus} \\ \beta = \frac{T - T_{solidus}}{T_{liquidus} - T_{solidus}} & \text{for } T_{solidus} < T < T_{liquidus} \\ \beta = 1 & \text{for } T > T_{liquidus} \end{cases} \quad (1)$$

β is 0 where the zone is totally solid, it is 1 where the zone is totally liquid. In Eq. (1), T is the local temperature and $T_{solidus}$ and $T_{liquidus}$ are the solid and liquid phase temperatures, respectively. The part of the domain below the first temperature is fully solid, while the part of the domain above the latter temperature is fully liquid. The melting occurs when the temperature is included between $T_{liquidus}$ and $T_{solidus}$. The

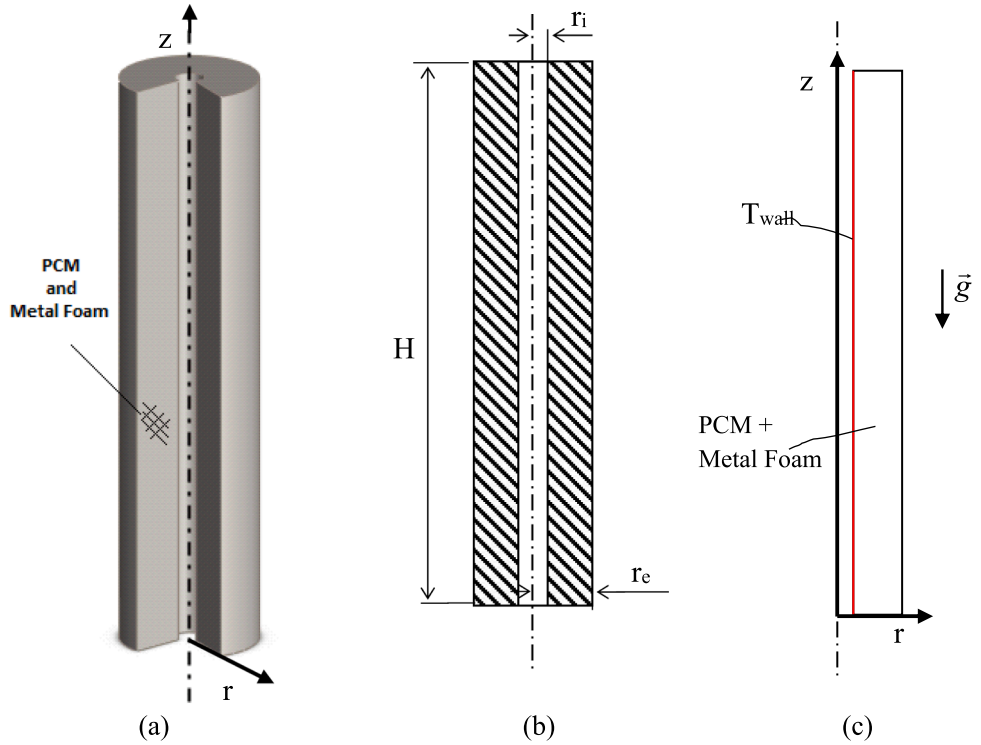

Fig. 1. Latent heat thermal energy storage system geometry: (a) sketch of the thermal energy storage, (b) geometrical characteristics and (c) boundary conditions and numerical domain.

description of the enthalpy-porosity method, during the melting or solidification, is completed considering a source term in the momentum equation which takes account of the solid part of the mixed zone. In fact, the mixed zone is modelled as a pseudo porous zone where the liquid fraction represents the porosity.

In the examined problem it is important to estimate by means the scale analysis, the order of magnitude of local temperature difference between foam, solid matrix, and PCM in solid and liquid phase with respect to total temperature difference. In a simple geometry as parallel channel with metal foam and PCM the inertia term for the metal component is $\rho_{mf} c_{mf} \frac{\Delta T_G}{t} V_{mf}$, where V_{mf} is the part of volume filled by the metal and it is equal to $(1-\varepsilon)V_t$, ΔT_G is of order magnitude of $(T_w - T_m)$. The local heat transfer at the interface between the metal and PCM is $A_{sf} h_{sf} (T_{mf} - T_p)$, where h_{sf} is the convective heat transfer coefficient, A_{sf} is the exchange area and $(T_{mf} - T_p)$ is the local difference of temperature between the metal and PCM. The balance between the inertia term and the local heat transfer is $(1-\varepsilon)\rho_{mf} c_p \frac{\Delta T_G}{t} \sim a_{sf} h_{sf} (T_{mf} - T_p)$, with $a_{sf} = A_{sf}/V_t$, and in the parallel channel system it is equal to $(2nl \cdot L_r)/(L_r^2 L_z)$, n is number of channels or cells. The dimensionless time, Fourier number, is $Fo = \alpha t / L_r^2$ and it results that $\frac{\Delta T_{mf,p}}{\Delta T_G} \sim \frac{(1-\varepsilon)\rho_{mf} c_{mf}}{a_{sf} h_{sf} t} = \frac{(1-\varepsilon)\rho_{mf} c_{mf}}{a_{sf} h_{sf}} \frac{\alpha_{mf}}{Fo L_r^2}$. Considering the a_{sf}value, it is $\frac{\Delta T_{mf,p}}{\Delta T_G} \sim \frac{(1-\varepsilon)\rho_{mf} c_{mf} (L_r^2 L_z)}{(2nlL_r) h_{sf}} \frac{\alpha_{mf}}{Fo L_r^2} = \frac{(1-\varepsilon)\rho_{mf} c_{mf} \alpha_{mf} L_z}{(2nlL_r) h_{sf} Fo}$ and assuming $L_z \sim L_r$, it is $\frac{\Delta T_{mf,p}}{\Delta T_G} \sim \frac{(1-\varepsilon) k_{mf}}{2nlFo h_{sf}}$. The worst condition is when there is only conduction at the interface and $h_{sf} \sim k_P/\delta_P$ with $\delta_P \sim \varepsilon L_r/n$, it is $\frac{\Delta T_{mf,p}}{\Delta T_G} \sim \frac{(1-\varepsilon)\varepsilon L_r k_{mf}}{2n^2 l Fo k_P}$.

For cylindrical geometry it is $l \sim L_r \sim L_z$ and $\frac{\Delta T_{mf,p}}{\Delta T_G} \sim \frac{(1-\varepsilon)\varepsilon k_{mf}}{2n^2 \cdot Fo \cdot k_P}$.

Furthermore, for a square channel, the term related to the number of cells is $(2n)^2$ and the fraction has an order of magnitude n^3, and in the cubic geometry, the number of cells is of order n^3 and the fraction has an order of n^4. If the number of pores per inch is equal to 20, it is $(20)^4$ then, the local thermal equilibrium is acceptable. Following this hypothesis, the local thermal equilibrium is assumed.

The following hypotheses are assumed in the present study:

1) A two-dimensional physical model is considered enclosed in two vertical coaxial cylinders.
2) The internal cylindrical surface is assumed isothermal and the external one is assumed adiabatic.
3) The Boussinesq approximation is used to simulate the natural convection of the liquid phase.
4) The PCM thermal properties are assumed constant. They are evaluated in the solid phase at 300 K, during the melting at 321 K and in the liquid phase at 335 K.
5) The metal foam is isotropic and homogenous and it is simulated as a porous media.

According to the hypothesis from 1) to 5) the governing equations are the following:

- The continuity equation

$$\frac{1}{r}\frac{\partial}{\partial r}(ru) + \frac{\partial w}{\partial z} = 0 \tag{2}$$

where u and w are the radial and axial velocity of the PCM in liquid phase, respectively, and r, z are the cylindrical coordinates.

- The momentum equations [35]:

$$\frac{\rho_p}{\varepsilon}\left(\frac{\partial u}{\partial t} + \frac{u}{\varepsilon}\frac{\partial u}{\partial r} + \frac{w}{\varepsilon}\frac{\partial u}{\partial z}\right)u = -\frac{\partial p}{\partial r} + \frac{\mu_p}{\varepsilon}\left(\frac{\partial^2 u}{\partial r^2} + \frac{1}{r}\frac{\partial u}{\partial r} - \frac{u}{r^2} + \frac{\partial^2 u}{\partial z^2}\right) + S_r \tag{3}$$

$$\frac{\rho_p}{\varepsilon}\left(\frac{\partial w}{\partial t} + \frac{u}{\varepsilon}\frac{\partial w}{\partial r} + \frac{w}{\varepsilon}\frac{\partial w}{\partial z}\right)u = -\frac{\partial p}{\partial r} + \frac{\mu_p}{\varepsilon}\left(\frac{\partial^2 w}{\partial r^2} + \frac{1}{r}\frac{\partial w}{\partial r} - \frac{u}{r^2} + \frac{\partial^2 w}{\partial z^2}\right) + S_z \tag{4}$$

where ρ_p is the density of the PCM and it depends on temperature assuming the Boussinesq approximation, μ_p is the viscosity of the liquid PCM, p is the pressure and vector S_r and S_z are the source terms defined as [35]:

$$S_r = \frac{(1-\beta)^2}{(\beta^3 + 0.001)^3} A_{mush} u + \frac{\mu_p}{K} u + \frac{C_F}{\sqrt{K}} \rho_p u \sqrt{u^2 + w^2} \tag{5}$$

$$S_z = \frac{(1-\beta)^2}{(\beta^3 + 0.001)^3} A_{mush} w + \frac{\mu_p}{K} w + \frac{C_F}{\sqrt{K}} \rho_p w \sqrt{u^2 + w^2} + \rho_p g \gamma (T - T_0) \tag{6}$$

It is important to analyze the terms of Eqs. (5)–(6). The term related to the enthalpy-porosity method is the first one and it simulates the presence of the solid part in the mixed zone. Therefore, β indicates the liquid fraction and 0.001 is assigned to avoid a division by zero when the liquid fraction tends towards zero [35]. A_{mush} is the mushy zone constant and it represents the velocity damping to zero in the solidification process [40]. The constant A_{mush} does not affect the behavior of the melting when there is a metal foam in the system. In fact, several simulations have been performed in order to evaluate the effect of the A_{mush} but they have shown that there are no correlation and the results are reported in Fig. 2. In Fig. 2a the results without foam are reported and the dependence is evident. The results with the presence of the metal foam in Fig. 2b, are not affected by the mushy constant value.

In this investigation, the value of mushy constant is assumed equals to 10^5 kg m^{-3} s^{-1}. The second and third terms simulate the presence of metal foam as a porous media. In fact, the second term is Darcy law and the third term is related to the Forchheimer law. The permeability of the porous media is indicated by K and inertial drag factoris C_F. For this investigation, their values are in sync with the following equations [59]:

$$K = 0.00073(1-\varepsilon)^{-0.224}\left(\frac{d_f}{d_p}\right)^{-1.11} d_p^2 \tag{7}$$

$$C_F = 0.00212(1-\varepsilon)^{-0.132}\left(\frac{d_f}{d_p}\right)^{-1.63} \tag{8}$$

with d_f and d_p the metal foam ligament diameter and the pore diameter, respectively. Another important quantity is the pore density ω which represents the number of pores across one inch, pores per inch (PPI). These characteristics are linked by [59]:

$$\frac{d_f}{d_p} = 1.18\sqrt{\frac{1-\varepsilon}{3\pi}}\left(\frac{1}{1 - e^{1(1-\varepsilon)/0.04}}\right) \tag{9}$$

$$d_p = \frac{0.0224}{\omega} \tag{10}$$

The last term in Eq. (6) takes account of the buoyancy effect, where T_0 is the reference temperature and γ represents the thermal expansion coefficient.

- The energy equation with local thermal equilibrium assumption is, [37]:

$$(\rho c)_{eff}\left(\frac{\partial T}{\partial t} + u\frac{\partial T}{\partial r} + w\frac{\partial T}{\partial z}\right) = k_{eff}\left[\frac{\partial}{\partial r}\left(\frac{1}{r}\frac{\partial}{\partial r}(rT)\right) + \frac{\partial^2 T}{\partial z^2}\right] - \varepsilon\rho_p H_L \frac{\partial \beta}{\partial t} \tag{11}$$

$(\rho c)_{eff}$is a weighted average value, [37]:

$$(\rho c)_{eff} = (1-\varepsilon)\rho_{mf} c_{mf} + \varepsilon\rho_p c_p \tag{12}$$

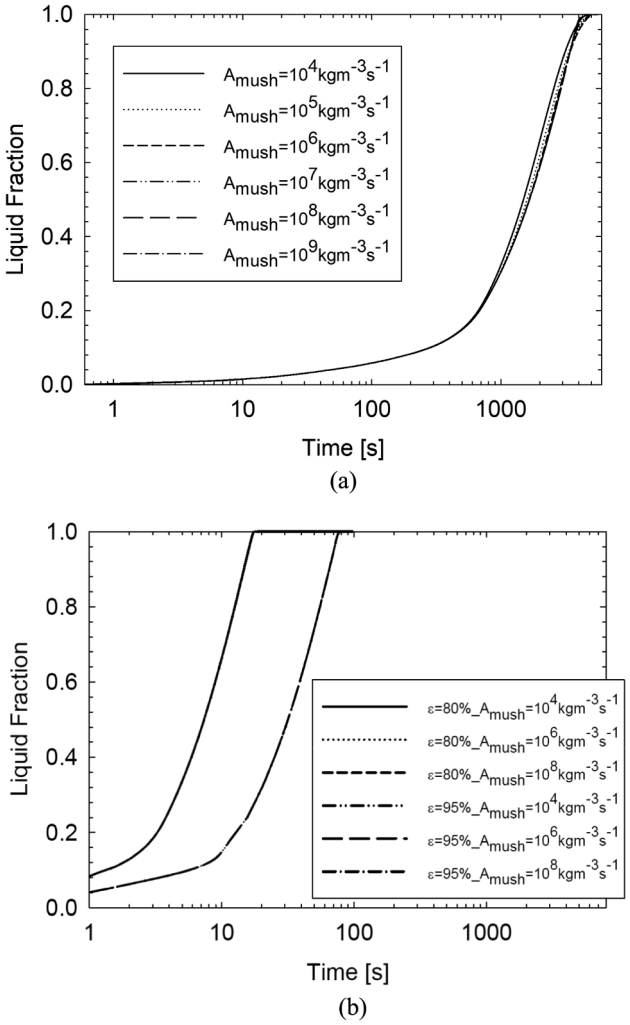

Fig. 2. Liquid fraction for different A_{mush} values: (a) CLEAN case and (b) PCM in aluminum foam.

In Eq. (12), ρ_{mf} and c_{mf} represent the metal foam density and specific heat, the metal foam porosity is ε and the density and specific heat of PCM are indicated by ρ_p and c_p. The effective thermal conductivity $k_{eff}$is evaluated as, [37]:

$$k_{eff} = (1 - \varepsilon)k_{mf} + \varepsilon k_p \tag{13}$$

with $k_{mf}$and k_p the metal foam and PCM thermal conductivities, respectively. In Eq. (8) H_L represents the latent heat of the PCM whereas t is the time.

In the present work, the paraffin RT58 of the Rubitherm [60] is the PCM and the metal foam is made of aluminum. The choice of aluminum foam is dictated by its relative low cost, and its lower density and weight, in relation to other materials.

Their thermo-physical properties are reported in Table 2. The melting behavior is assumed linear as employed in [26–28,37].

To assess the efficiency of the system, a dimensionless parameter is employed, as given by Yang et al. [53]. It represents the energy stored in each assigned time step:

$$q = \frac{E_t - E_{t-\Delta t}}{H_L} \tag{14}$$

$E_t - E_{t-\Delta t}$ represents the specific enthalpy variation in the time step Δt, with H_L the PCM latent heat of fusion and q is a performance dimensionless parameter.

3. Numerical model

The governing Eqs. (2)–(4) and (11) are solved by means of Ansys-Fluent commercial code [61] which uses the finite volume method to discretize the problem. The SIMPLE algorithm is employed for the pressure-velocity coupling; PRESTO algorithm is used for the pressure calculation. The high order term relaxation is set equal to 0.75 for all variables, in order to avoid the numerical instability of the system. A transient analysis is performed with a time step size equal to 0.05 s. The convergence errors are assumed equal to 10^{-5}, for continuity and momentum equation, and 10^{-8}, for energy equation. The numerical grid is set of quadrilateral cells having a small size near the boundary and a large size in the center of the grid with a maximum size ratio equal to 2.

In order to check the accuracy of the results, a grid independency analysis is performed with five discretization: 4×10, 12×30, 16×40, 20×50, 40×100 nodes. The melting dimensionless time, Fourier number, is considered to assess the grid independence comparing the values of the liquid fraction for each mesh and the results are given in Fig. 3. A grid with 20×50 nodes is employed to perform the study and it represents the best compromise between the solution accuracy and computing time.

A validation test comparing the model with the work of Krishnan et al. [54] is carried out. The comparison is accomplished using the same geometry, dimensions and limit conditions (initial and boundary conditions), as well as the same properties and numerical grid given in [54].

In Table 3 the deviation between the Krishnan et al [54] and the present model is compared for different Fourier numbers, Fo. It shows that the maximum deviation is lower than 3%. As shown in Fig. 4, where T^* is the non-dimensional temperature, X^* is the non-dimensional r length at midway of the numerical domain, Fo is the non-dimensional time:

$$T^* = \frac{T - T_i}{T_w - T_i} \qquad X^* = \frac{r}{L_r} \qquad Fo = \frac{tk_p}{\rho_p c_p L_r^2} \tag{15}$$

where T_w is the wall temperature and T_i is the initial temperature set to 300 K. L_r is a characteristic length of the system along the radial direction. The reliability of the model is ensured.

4. Results and discussions

4.1. Scale analysis

Before presenting the results, a scale analysis is presented to explain the melting phenomenon inside the system. The order of magnitude estimation of the involved physical parameters can be provided by means of the scale analysis. It allows to compare parameters such as time, length scales in the different heat transfer regimes in the melting of PCM in porous medium (metal foam) in the considered geometry and

Table 2
Thermal proprieties of the paraffin RT58.

Properties	Paraffin RT58 [52]	Aluminum foam [53]
Density [kg/m^3]	840	2719
Specific Heat [J/kg K]	2100	871
Thermal Conductivity [W/m K]	0.2	202.4
Dynamic Viscosity [kg/m s]	0.0269	–
Thermal expansion coefficient [1/K]	0.00011	–
Melting Heat [J/kg]	180,000	–
Solidus Temperature [K] (start melting temperature value)	321	–
Liquidus Temperature [K] (end melting temperature value)	335	–

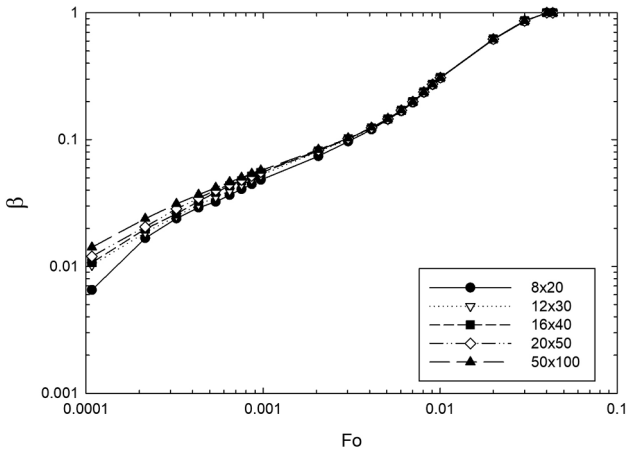

Fig. 3. Analysis of the dependence of results from the grid.

Table 3
Model Validation.

Fo	*T** [54]	*T** present model	*Error* [%]
0.4	0.4854	0.4903	1.01
0.6	0.5719	0.5634	1.49
1.2	0.6011	0.5851	2.66

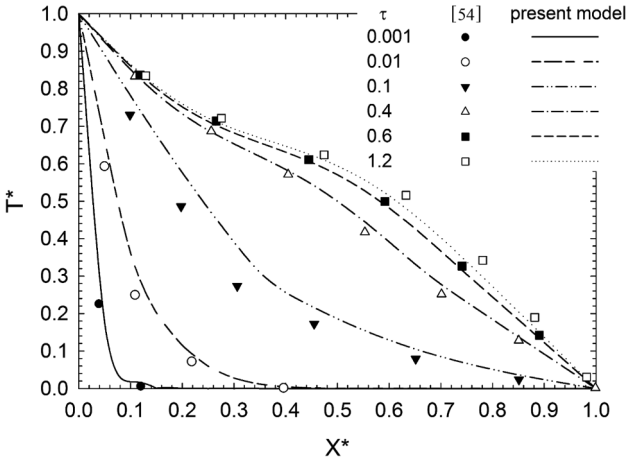

Fig. 4. Comparison with the results from Krishnan et al. [54] (points) and present data (lines). T* is the dimensionless temperature and X* is the dimensionless length at half height.

thermal boundary conditions. The analysis follows the one given in [62–65] and it starts from the governing equations:

$$\frac{1}{r}\frac{\partial}{\partial r}(ru) + \frac{\partial w}{\partial z} = 0 \tag{16}$$

$$u = -\frac{K}{\mu_p}\frac{\partial p}{\partial r} \tag{17}$$

$$w = -\frac{K}{\mu_p}\left[\frac{\partial p}{\partial z} - \rho_p g\gamma(T - T_m)\right] \tag{18}$$

$$(\rho c)_{eff}\frac{\partial T}{\partial t} + \rho_p c_p\left(u\frac{\partial T}{\partial r} + w\frac{\partial T}{\partial z}\right) = k_{eff}\left[\frac{\partial}{\partial r}\left(\frac{1}{r}\frac{\partial}{\partial r}(rT)\right) + \frac{\partial^2 T}{\partial z^2}\right] - \varepsilon\rho_p H_L\frac{\partial \beta}{\partial t} \tag{19}$$

From Eqs. (17) and (18) it results

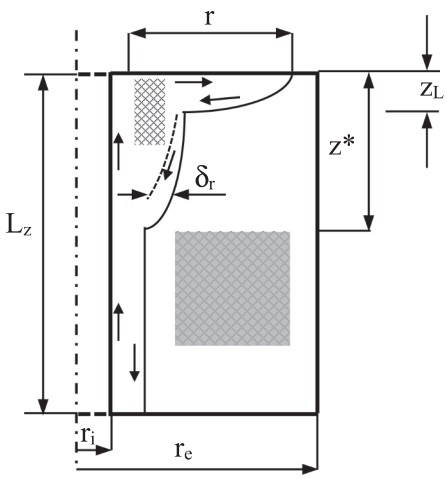

Fig. 5. Cylindrical enclosure and geometrical lengths in scale analysis.

$$\frac{\partial u}{\partial z} - \frac{\partial w}{\partial r} = -\frac{K}{\mu_p}\rho_p g\gamma\frac{\partial T}{\partial r} \tag{20}$$

The external temperature of the internal tube is assigned and equal to T_w and greater than the melting temperature of PCM, T_m.

At the beginning, the process is dominated by the diffusion [65] and $u \sim w \sim 0$; consequently, the terms in energy Eq. (19), with reference to Fig. 5, are

$$(\rho c)_{eff}\frac{\Delta T}{t};\ k_{eff}\frac{\Delta T}{L_r^2},\ k_{eff}\frac{\Delta T}{L_z^2},\ \varepsilon\rho_p H_L\frac{\beta}{t} \tag{21}$$

with $\beta \sim D/L_r$ and L_r as reference length along the radial direction, r_e.

At the beginning, diffusion and melting have the same order of magnitude (OoM) and

$$k_{eff}\frac{\Delta T}{L_r^2} \sim \varepsilon\rho_p H_L\frac{D/L_r}{t} \tag{22}$$

with Fourier number and Stefan number defined as:

$$Fo = \frac{\alpha_{eff}\, t}{L_r^2} \tag{23}$$

$$Ste = \frac{c_p \Delta T}{H_L} \tag{24}$$

It is

$$\frac{D}{L_r} \sim \frac{Ste \times Fo}{\varepsilon}\frac{(\rho c)_{eff}}{\rho_p c_p} \tag{25}$$

For $\beta \sim 1$, $D \sim L_r$, it is

$$\left(\frac{D}{L_r}\right)^2 \sim \frac{Ste \times Fo}{\varepsilon}\frac{(\rho c)_{eff}}{\rho_p c_p} \Rightarrow \frac{D}{L_r} \sim \left[\frac{Ste \times Fo}{\varepsilon}\frac{(\rho c)_{eff}}{\rho_p c_p}\right]^{1/2} \tag{26}$$

For $(D/L_r) \sim \beta$, in diffusion region with $D < L_r$ but $L_r \sim D$, it is

$$\left(\frac{D}{L_r}\right)^3 \sim \frac{Ste \times Fo}{\varepsilon}\frac{(\rho c)_{eff}}{\rho_p c_p} \Rightarrow \frac{D}{L_r} \sim \left[\frac{Ste \times Fo}{\varepsilon}\frac{(\rho c)_{eff}}{\rho_p c_p}\right]^{1/3} \tag{27}$$

In a general form it is

$$\frac{D}{L_r} \sim \left[\frac{Ste \times Fo}{\varepsilon}\frac{(\rho c)_{eff}}{\rho_p c_p}\right]^n \text{ with } n = 1, \frac{1}{2}, \frac{1}{3} \tag{28}$$

It is interesting to observe that, it should be:

$$\frac{Ste \times Fo}{\varepsilon}\frac{(\rho c)_{eff}}{\rho_p c_p} \leqslant \frac{D}{L_r} \leqslant \left[\frac{Ste \times Fo}{\varepsilon}\frac{(\rho c)_{eff}}{\rho_p c_p}\right]^{1/3} \tag{29}$$

After the diffusion region there is a transition/mixed region [62–65]. At the commencement of melting, there is a balance between the inertia and diffusion and from energy Eq. (19) it is:

$$(\rho c)_{eff}\frac{\Delta T}{t} \sim k_{eff}\frac{\Delta T}{L_r^2} \Rightarrow t \sim \frac{L_r^2}{\alpha_{eff}} \text{ and } \delta_r \sim (\alpha_{eff} t)^{1/2} \text{ with } L_r = \delta_r \tag{30}$$

For melting stage, from Eq. (16) it is:

$$\frac{u}{L_r} \sim \frac{w}{L_z} \tag{31}$$

In this region, in a layer of thickness δ_r

$$\frac{u}{\delta_r} \sim \frac{w}{L_z} \Rightarrow \frac{u}{w} \sim \frac{\delta_r}{L_z} \tag{32}$$

Moreover, from Eq. (20) the orders of magnitude are:

$$\frac{u}{L_z}, \frac{w}{\delta_r}; \frac{K}{\mu_p}\rho_p g\gamma\frac{\Delta T}{\delta_r} \tag{33}$$

it is

$$\frac{u}{w}\frac{\delta_r}{L_z}, 1; \frac{K}{\mu_p}\rho_p g\gamma\frac{\Delta T}{w} \Rightarrow \frac{\delta_r^2}{L_z^2}, 1; \frac{K}{\mu_p}\rho_p g\gamma\frac{\Delta T}{w} \tag{34}$$

For $\delta_r \ll L_z$ it is:

$$w = \frac{K}{\mu_p}\rho_p g\gamma\Delta T \tag{35}$$

From energy Eq. (19), taking into account only the liquid part, it is in terms of OoM

$$(\rho c)_{eff}\frac{\Delta T}{t}, \rho_p c_p u\frac{\Delta T}{L_r}, \rho_p c_p w\frac{\Delta T}{L_z}; k_{eff}\frac{\Delta T}{L_r^2}, k_{eff}\frac{\Delta T}{L_z^2} \tag{36}$$

the diffusion is negligible, and the inertia term is compared to the convection along the axial direction:

$$(\rho c)_{eff}\frac{\Delta T}{t} \sim \rho_p c_p w\frac{\Delta T}{L_z} \tag{37}$$

Then Eq. (37) allows to evaluate the time, t_c, needed to start the convection:

$$t_c \sim \frac{(\rho c)_{eff}}{\rho_p c_p}\frac{L_z}{w} \tag{38}$$

After this time, the significant terms are the convection along z direction and diffusion along radial direction:

$$\rho_p c_p w\frac{\Delta T}{L_z} \sim k_{eff}\frac{\Delta T}{L_r^2} \tag{39}$$

and it results in:

$$w \sim \frac{k_{eff}}{\rho_p c_p}\frac{L_z}{L_r^2} = \alpha_{eff}\frac{(\rho c)_{eff}}{\rho_p c_p}\frac{L_z}{L_r^2} \tag{40}$$

from Eqs. (35) and (40)

$$\frac{K}{\mu_p}\rho_p g\gamma\Delta T \sim \alpha_{eff}\frac{(\rho c)_{eff}}{\rho_p c_p}\frac{L_z}{L_r^2} = \alpha_{eff}\frac{(\rho c)_{eff}}{\rho_p c_p}\left(\frac{L_z}{L_r}\right)^2\frac{1}{L_z} \tag{41}$$

with:

$$Ra_{K,L_z} = \frac{\rho_p g\gamma\Delta T(K\ L_z)}{\mu_p\alpha_p} \tag{42}$$

From Eq. (42), it is, as general relation between the two characteristic lengths along radial and axial directions and according to [[64], Eq. (8)] for pure PCM,

$$\frac{L_r}{L_z} \sim \left(\frac{k_{eff}}{k_p}\right)^{\frac{1}{2}} Ra_{K,L_z}^{-\frac{1}{2}} \tag{43}$$

In the transition region it is $L_r \sim \delta_r \sim D$

$$\frac{\delta_r}{L_z} \sim \left(\frac{k_{eff}}{k_p}\right)^{\frac{1}{2}} Ra_{K,L_z}^{-\frac{1}{2}} \Rightarrow \frac{\delta_r}{L_r} \sim \frac{L_z}{L_r}\left(\frac{k_{eff}}{k_p}\right)^{\frac{1}{2}}\frac{1}{Ra_{K,L_z}^{1/2}} \tag{43a}$$

Eq. (43a) indicates that for assigned Rayleigh number, porous medium and PCM the greater the aspect ratio the greater the thickness δ_r and the convection is weak inside the PCM.

With $L_z \sim z^*$ and

$$Ra_{K,z^*} = \frac{\rho_p g\gamma\Delta T(K\ z^*)}{\mu_p\alpha_p} = Ra_{K,L_z}\frac{z^*}{L_z} \tag{44}$$

Eq. (43) provides

$$\frac{\delta_r}{z^*} \sim \left(\frac{k_{eff}}{k_p}\right)^{\frac{1}{2}} Ra_{K,z^*}^{-\frac{1}{2}} \tag{45}$$

Considering Eqs. (28) with $\delta_r \sim D$, (43) and (44) in Eq. (45) it results in:

$$\frac{z^*}{L_z} \sim \left[\frac{Ste \times Fo}{\varepsilon}\frac{(\rho c)_{eff}}{\rho_p c_p}\right]^{2\gamma}\left(\frac{k_{eff}}{k_p}\right)^{\frac{1}{2}} Ra_{K,L_z}^{\frac{1}{2}} \tag{46}$$

As highlighted by Lorente et al. [65] for high enough Rayleigh numbers in the upper part of the reservoir, a distinct layer of shallow liquid is determined, as shown in Fig. 5. In this zone z_L is the vertical thickness and r is the penetration radius. The conservation of mass demands:

$$\frac{u}{r} \sim \frac{w}{z_L} \tag{47}$$

The momentum equation (20), with the dominant component along r, gives

$$\frac{u}{z_L} = \frac{K}{\mu_p}\rho_p g\gamma\frac{\Delta T}{r} \tag{48}$$

Moreover, the balance between diffusion and latent heat absorbed at melting front can be written as:

$$k_{eff}\frac{\Delta T}{z_L} \sim \varepsilon\rho_p H_L\frac{z_L}{t} \Rightarrow z_L \sim \left(t\frac{k_{eff}\Delta T}{\varepsilon\rho_p H_L}\right) \tag{49}$$

Considering the energy Eq. (19) for liquid PCM inside the slender cavity zone, the convective terms along the radial, r, direction is balanced by the diffusion terms along the axial, z, direction, it results in:

$$\rho_p c_p u\frac{\Delta T}{r} \sim k_{eff}\frac{\Delta T}{z_L^2} \tag{50}$$

And combining Eqs. (50) with (48) and (49), it is evaluated the radial scale of penetration r

$$r \sim \left(t\frac{k_{eff}\Delta T}{\varepsilon\rho_p H_L}\right)^{\frac{1}{2}}\left(\frac{k_p}{k_{eff}}\frac{\rho_p g\gamma\Delta TK}{\alpha_p\mu_p}\right)^{\frac{1}{3}} = \left(t\frac{k_{eff}\Delta T}{\varepsilon\rho_p H_L}\right)^{\frac{1}{2}}\left(\frac{k_p}{k_{eff}}Ra_{K,r}\right)^{\frac{1}{3}} \tag{51}$$

With

$$Ra_{K,r} = \frac{\rho_p g\gamma\Delta TK}{\alpha_p\mu_p}$$

The ratio between the two length scales in the horizontal slender layer provides

$$\frac{z_L}{r} \sim \left(\frac{k_p}{k_{eff}}\right)^{\frac{1}{3}} Ra_{K,r}^{-\frac{1}{3}} \tag{52}$$

Eq. (52) agrees with the results given by Lorente et al. [65].

It is interesting to observe from Eqs. (47) and (52)

$$\frac{w}{u} \sim \frac{z_L}{r} \tag{53}$$

that the velocity along the axial direction is of the same order of magnitude of the slender thickness.

Moreover,

$$Ra_{K,r} = Ra_{K,L_z}\frac{r}{L_z} \sim Ra_{K,L_z}\frac{L_r}{L_z} \tag{54}$$

and from Eqs. (52) and (54)

$$\frac{z_L}{r} \sim \left(\frac{k_p}{k_{eff}}\right)^{\frac{1}{3}}\frac{L_z}{L_r}Ra_{K,L_z}^{-1/3} \tag{55}$$

4.2. Numerical simulation results

The analysis is accomplished assuming a wall temperature on the external surface of the inner cylinder, T_w, equal to 350 K and the internal surface of the external cylinder adiabatic. The simulations are performed employing, in all cases, a PPI value of 20 and for different porosity values of 0.80, 0.85, 0.90, 0.95, 0.97 and 0.99 and three value of the difference between external and internal radius, Δr = 10 mm, 20 mm and 30 mm.

The average value of liquid fraction and average temperature profiles, as a function of time, are presented in Fig. 6, for pure PCM (CLEAN) case, and PCM in metal foam with several porosity values, from 80% to 99%, for assigned difference between the external and internal radii (r_e-r_i) equal to 10 mm, in Fig. 6a and b, and three different Δr, in Fig. 6c and d.

The liquid fraction can be assessed as the ratio between the volume of the liquid PCM in the mixed region and the total volume of the mixed region. In Fig. 6a and c, the liquid fraction profiles are the average liquid fraction inside the whole system, therefore they represent the total volume of the liquid PCM inside the system. The diagrams, in Fig. 6a, allow to compare the CLEAN case with the ones with porosity here considered from 0.8 to 0.99. In Fig. 6a, the first difference between the curves is the shift of the curves, which indicates that the curve with the porosity equal to 80%, in Fig. 6a, has the fastest melting process among all considered cases. This can be explained in terms of the presence of the metal foam which increases the thermal diffusivity of the whole system, and consequently, the thermal disturbance diffuses faster. It is observed that the melting time, which is the time required to obtain the complete melting, for the CLEAN case is greater than 4000 s, while it is about 18 s for the case with the aluminum foam with the lowest porosity of 80%. In Fig. 6a, it is observed that the porosity increase delays the melting, i.e, it causes a slower melting and, consequently, the liquid fraction increases less quickly as the porosity increases. The effect of the metal foam is weaker as the porosity increases and the lowest melting velocity is attained for a porosity equal to 1, i.e., the CLEAN case. The average liquid fraction diagrams present similar curves and a first linear trend is observed with a greater slope for the case with PCM in metal foam, in Fig. 6a. The second part of the curves shows an increase in the slope, in Fig. 6a for the logarithmic scale. Finally, there is a small part near the end where the slope tends to decrease both for the CLEAN case and for the case with PCM in metal foam. These three steps represent the average melting process inside the thermal storage. In the first step the PCM is still solid and the melting occurs near the heated wall. In the second step the PCM has a large portion of the volume that is undergoing the melting process. During the third step the melting is nearly completed.

In Fig. 6b, average temperature profiles as a function of time, are compared and three regions are detected along the diagrams relating to

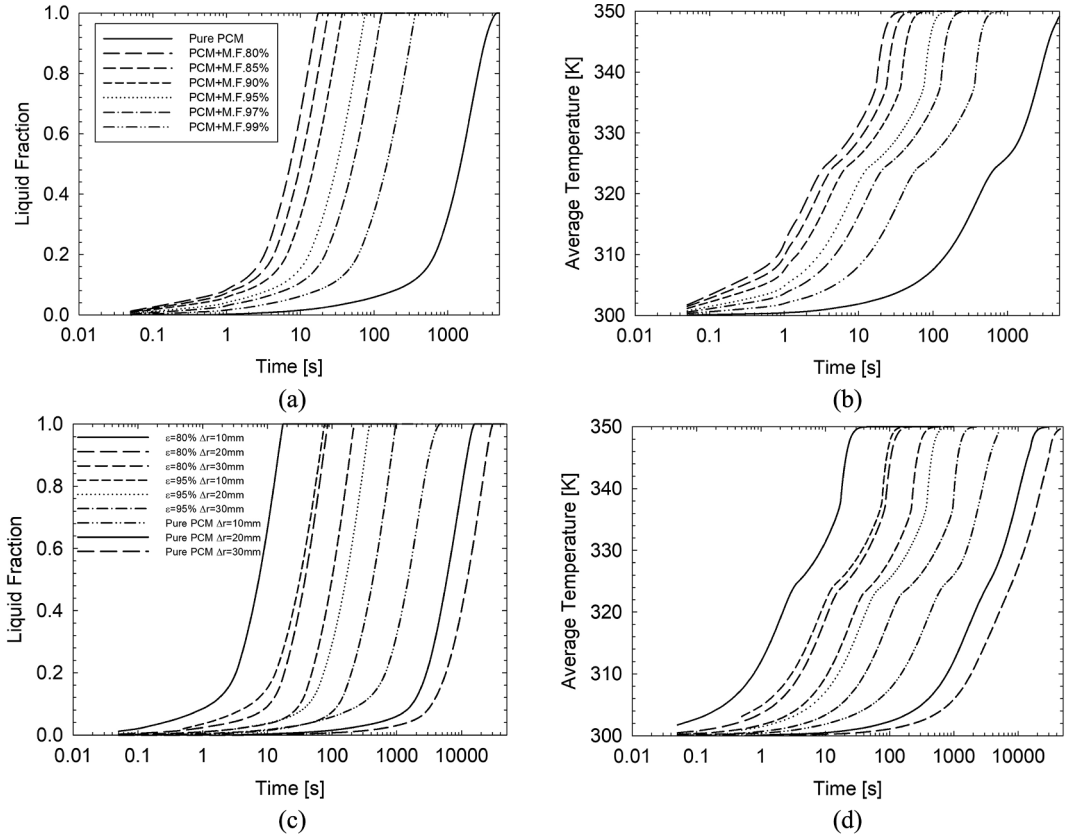

Fig. 6. Values of (a) average liquid fraction and (b) average temperature as a function of time for pure PCM or CLEAN case and PCM in aluminum foam with a porosity from 80% to 99%, for ($r_e - r_i$) = Δr = 10 mm; (c) average liquid fraction and (d) average temperature as functions of time for the cases with PCM in aluminum foam with a porosity of 80% and 95% and CLEAN (pure PCM) for Δr = 10 mm, 20 mm and 30 mm.

the CLEAN case and the aluminum foam cases, with the porosity from 80% to 99%. The three regions correspond to the ones identified for the liquid fraction, in Fig. 6a, with the first region relating to a fully conductive regime, without melting, the second region with the melting, and the third region with an almost completely melted region. Porosity affects the heat transfer behaviors by means of effective thermal conductivity and diffusivity, as shown in Eq. (13) and in energy Eq. (11). In fact, when the porosity increases, the effective thermal conductivity, together with the thermal diffusivity, decreases as indicated in Eq. (13). For this reason, more time is needed to arrive at the final temperature value, consequently delaying melting for higher porosity, conversely, it is observed that the lower the porosity, the lower the melting time. This depends also on the lesser PCM quantity and the higher effective diffusivity value which induces lower temperature differences inside the reservoir.

Fig. 6c and d, show that, increase in the melting time, is attributable to variations in the volume of storage, liquid fraction, as well as the average temperature, thereof. Trends of the curves are similar for all cases, but with an increase in the slope decreasing the difference Δr. It is of importance to note the relationship between diagrams in Fig. 6c and d, with table 4, where the melting time for the three $\Delta r = 10$ mm, 20 mm, and 30 mm, are indicated. For the case with PCM and foam, the melting time increases 5 times passing from $\Delta r = 10$ mm to $\Delta r = 20$ mm and about 13 times passing from $\Delta r = 10$ mm to $\Delta r = 30$ mm whereas it is 2.5 times passing from $\Delta r = 20$ mm to $\Delta r = 30$ mm. In the CLEAN cases, the ratio is lower mainly between $\Delta r = 10$ mm and $\Delta r = 30$ mm which is about the half of the previous case with PCM and foam. For assigned Δr, the ratio between the melting times of the cases with PCM and foam, with porosity equal to 80% and 95%, is constant. This shows that during the melting process, the conduction is significantly dominant, and the value of the ratio stands at about 4.4. This value is almost equal to the reciprocal of the ratio between the effective conductivities for the porosities equal to 80% and 95%, which are equal to about $40\,W\,K^{-1}\,m^{-1}$ and about $10\,W\,K^{-1}\,m^{-1}$, respectively. The ratios between the CLEAN cases and with PCM and foam, decrease, as Δr increases which point to an increase in natural convection related to a Δr increase. This ratio is smaller for higher porosity values.

Local analysis by means of liquid fraction, temperature and stream function fields facilitate an understanding of the differences between the behaviors of the CLEAN case and the one with metal foam, at lowest porosity of 0.8. In Fig. 7, the liquid fraction for pure PCM (CLEAN case) and PCM in metal foam, with a porosity equal to 0.8, is shown for three different times, referring to the melting times, t_m, $\tau = t/t_m = 1/100$, 1/4 and 1/2, and for $\Delta r = 10$ mm, 20 mm and 30 mm. The liquid phase is placed to behind the curve at 0.98, on the left of the pink line. The solid phase is placed before the line at 0.05, to the right of the blue line. The other colors indicate the mushy zone. The different shapes of the melting zone depend on the balance between the conduction phenomenon and the natural convection phenomenon as elucidated in the scale analysis. In fact, for the CLEAN case, after a few seconds, the natural convection is dominant, but for the case with metal foam, the conduction prevails, and the natural convection is not present or is negligible also for the largest reservoir, as shown in the fields given in Fig. 7f.

Table 4
Melting time in seconds, s, for Clean and PCM with foam for two porosity values.

Δr [mm]	ε = 0.80	ε = 0.95	Clean
10	17.5 s	77 s	4600 s
20	86.5 s	381 s	15780 s
30	220 s	973 s	30350 s

In details, in Fig. 7a, some liquid fraction distributions for the CLEAN case at $\Delta r = 10$ mm, which corresponds to an aspect ratio, $(r_e - r_i)/H = 0.10$, are reported at 46 s, 1150 s, and 2300 s. The first distribution, after 46 s, shows that the liquid fraction is very close and parallel to the internal heated cylinder, the melting zone is vertical with a very small and uniform liquid thickness. Then at the early stages, the regime is only conductive. This is in agreement with the scale analysis for the conduction/diffusion region. After that, in Fig. 7a, the natural convection becomes dominant, causing a bending of the melting zone. In fact, after 1150 s the liquid fraction shows that, in the upper zone, natural convection develops and the melted zone is very similar to the sketch given in Fig. 5, increasing the time the melting develops along the axial direction, and filling the breadth along the radial direction. At 2300 s the melt is almost present in the half reservoir and the mushy zone is in the other part of the volume. A completely different characterization of the melting zone is observed in Fig. 7d, for PCM and metal foam with $\Delta r = 10$ mm. This is due to the fact that the phase change is uniform along the vertical direction, for all times. This implies that significant reduction in the melting time is linked to effective thermal diffusivity increases, whereas, the convective motion is negligible. For higher Δr, equal to 20 mm and 30 mm, in both cases with and without foam, the phenomenological aspects are the same. The development of liquid fraction, reported in Fig. 7b and c, shows, for the CLEAN case, at the early stages, in Fig. 7b. The field develops in a similar way as the previous case with a lower aspect ratio. This indicates that the motion inside the melt close to the inner tube is negligible and the phenomenon is mainly conductive. Moreover, it is similar to a semi-infinite solid and one-dimensional along the radial direction. The natural convection and the subsequent melting process are less developed with respect to the previous case because there is more mass and the time to complete the melting is higher than the one with lower aspect ratio. From those fields it seems that the melting process along the z direction starts when the upper melting zone reaches the external adiabatic surface. This is in agreement with the scale analysis related to the results given in Eqs. (45) and (46). In fact, at the last considered time, for the three CLEAN cases, in Fig. 7a–c, the slender cavity is developing downward. Also, for larger aspect ratio values, in the case with metal foam, the melting process is dominated by diffusion, as it is noted in Fig. 7e and f, and the natural convection seems negligible.

Temperature distribution as a function of time is similar to the liquid fraction fields, as shown in Fig. 8. In this figure temperature fields are given for three periods, with reference to the melting time, $\tau = t/t_m = 1/100$, 1/4 and 1, and for $\Delta r = 10$ mm, 20 mm and 30 mm. Indeed, the CLEAN case exhibits a uniform temperature field at the beginning, with vertical isotherm lines, as shown in Fig. 8a, for $\Delta r = 10$ mm and $t = 46$ s. Later, the isotherm lines tend to bend because of the arising of natural convection, as shown in the frames for $t = 1150$ s and 4600 s. Nevertheless, in the case with the metal foam the temperature field, in Fig. 8d, presents vertical isotherms and moves in the radial direction, confirming that the conduction is prevalent during the phase change. In Fig. 8b and c, there are the temperature fields for $\Delta r = 20$ mm and 30 mm. However, the temperature fields show the distribution also inside the solid zone in the PCM, in Fig. 8a–c, and in the PCM in the metal foam, in Fig. 8d–f. The fields confirm that the initial stage is diffusive, as shown in the fields at lower time and they are practically one-dimensional. At 158 s and 303 s, in Fig. 8b and c, respectively, the incipient convection regime is started, and higher penetration is developing on the top. The temperature distribution in the solid zone presents some gradients due to the heat conduction. For the lower aspect ratio and pure PCM, for $t = 1150$ s, in Fig. 8a, the convective regime is dominant, where the temperature distribution indicates that almost all points are close to the lower melting temperature. In the geometry with higher aspect ratio, the temperature presents distributions that allow to describe the development of the slender cavity on the top region as clearer. The cases with foam, in Fig. 8d–f, demonstrate that the fields are one-dimensional. The

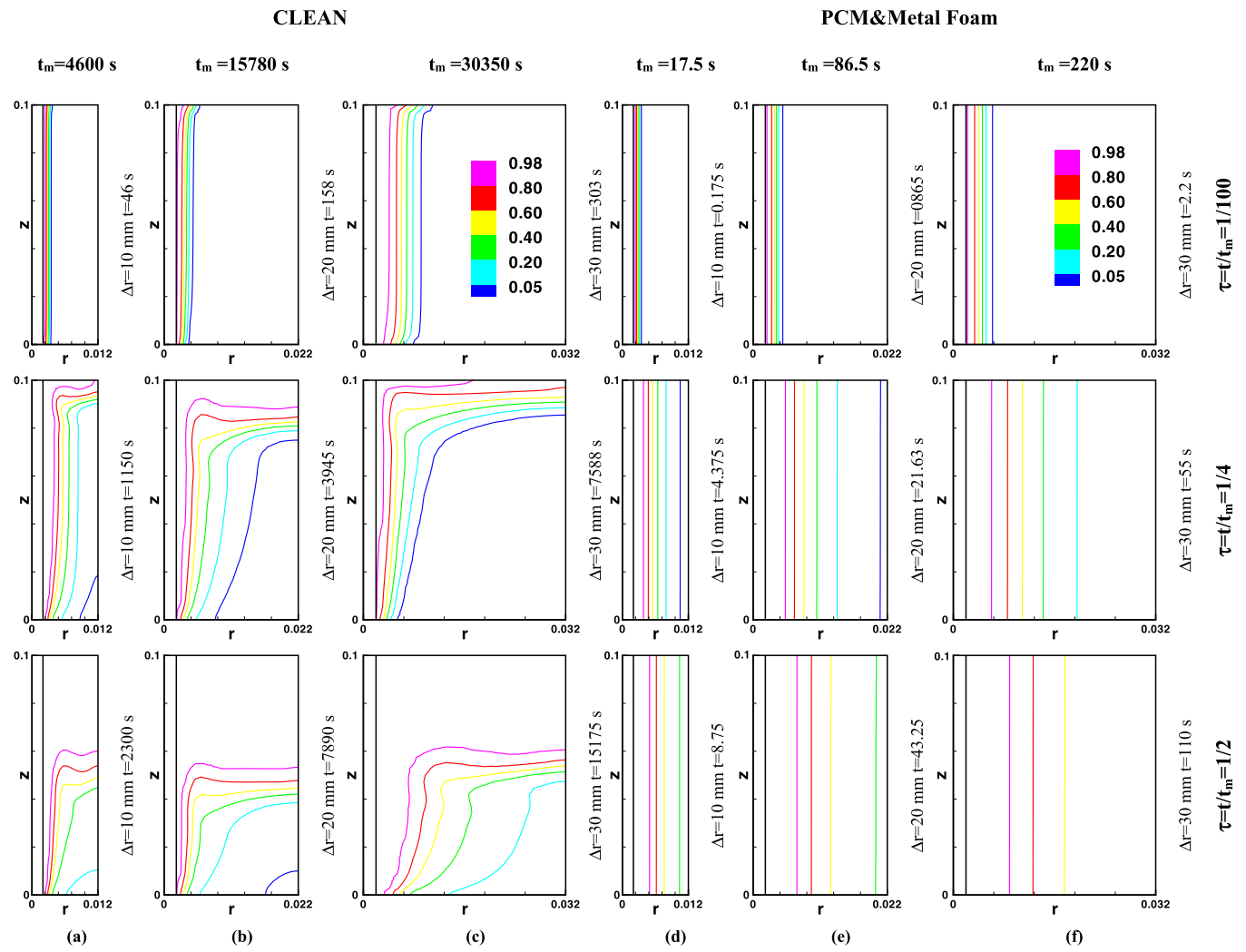

Fig. 7. Liquid fraction fields for Clean and PCM with metal foam, three radius differences, Δr = 10, 20 and 30 mm and three different time as fraction of melting time τ = t/tm.

dominant effect is only conductive with negligible natural convection for both aspect ratios.

Another aspect related to the melting process is the analysis of stream function fields, reported in Fig. 9. Their trends confirm the previous considerations. In the CLEAN case for Δr = 10 mm, in Fig. 9a, the stream functions are parallel only at the onset, for t = 46 s (τ = 0.01), because the natural convection effect is negligible, but after they tend to bend in the melting and liquid zones due to the natural convection effect, as shown for t = 1150 s (τ = 1/4) and 4600 s (τ = 1). The same consideration seems to hold for Δr = 20 mm and 30 mm, in Fig. 9b and c. In agreement with the scale analysis, given in the previous section, the different configurations in the melting process are observed mainly in the clean cases, with pure PCM. In Fig. 9a–c, the development of natural convection that starts from the slender cavity and after involves the entire cavity. In the case with metal foam, not reported here, the stream functions are very small, thus, implying that they may not have physical explanations.

In Fig. 10 the parameter q, as a function of time for different porosity values and CLEAN case, is given. The thermal parameter q is defined in Eq. (14), with reference to an assigned time range, Δt, and it represents the stored energy referred to the melting latent heat. It increases in tandem with the speed of the fusion process. In this figure, the results show that, the presence of metal foam improves the parameter q. Nevertheless, the trend is the same for all cases, except for the final stage, where the CLEAN case presents a collapse of q greater than the cases with metal foam. Moreover, it is observed that, without a porous medium (the CLEAN case), the q value is less than 1 for all the storage process here considered, both in the melting and sensible heating phases. In the cases with porous medium it is observed that q > 1 for the storage process with the porosity equal to 0.8, 0.85 and 0.9, whereas q presents values lower than 1 for ε = 0.95 after Fo = 0.01 (t = 22 s) and for ε = 0.97 after Fo = 0.021 (t = 8 s).

The analysis is completed considering two additional cases related to the reservoir filled with pure PCM in a reduced volume of the reservoir. The volume of these two cases is the 80% of the volume of the previous analyzed cases. To have the same amount of PCM, there is for the case with a porosity equal to 80%. The volume reduction in one case is obtained with the height of the reservoir equal to the 80% of the previous cases and in the other case reducing the base area of the 80% of the previous cases. The comparison is accomplished in terms of average temperature profiles, reported in Fig. 11, as a function of the time. It is observed that for the considered volume reduction, a higher melting time is realized for the lower height. This can be due to a lesser effect of the natural convection and a minor energy input. For the lower base area case, the average temperature profile presents lower melting time due to the lower value of the volume with the same energy input. However, the order of magnitude of the melting time, in both cases, is about the same with the CLEAN case with pure PCM.

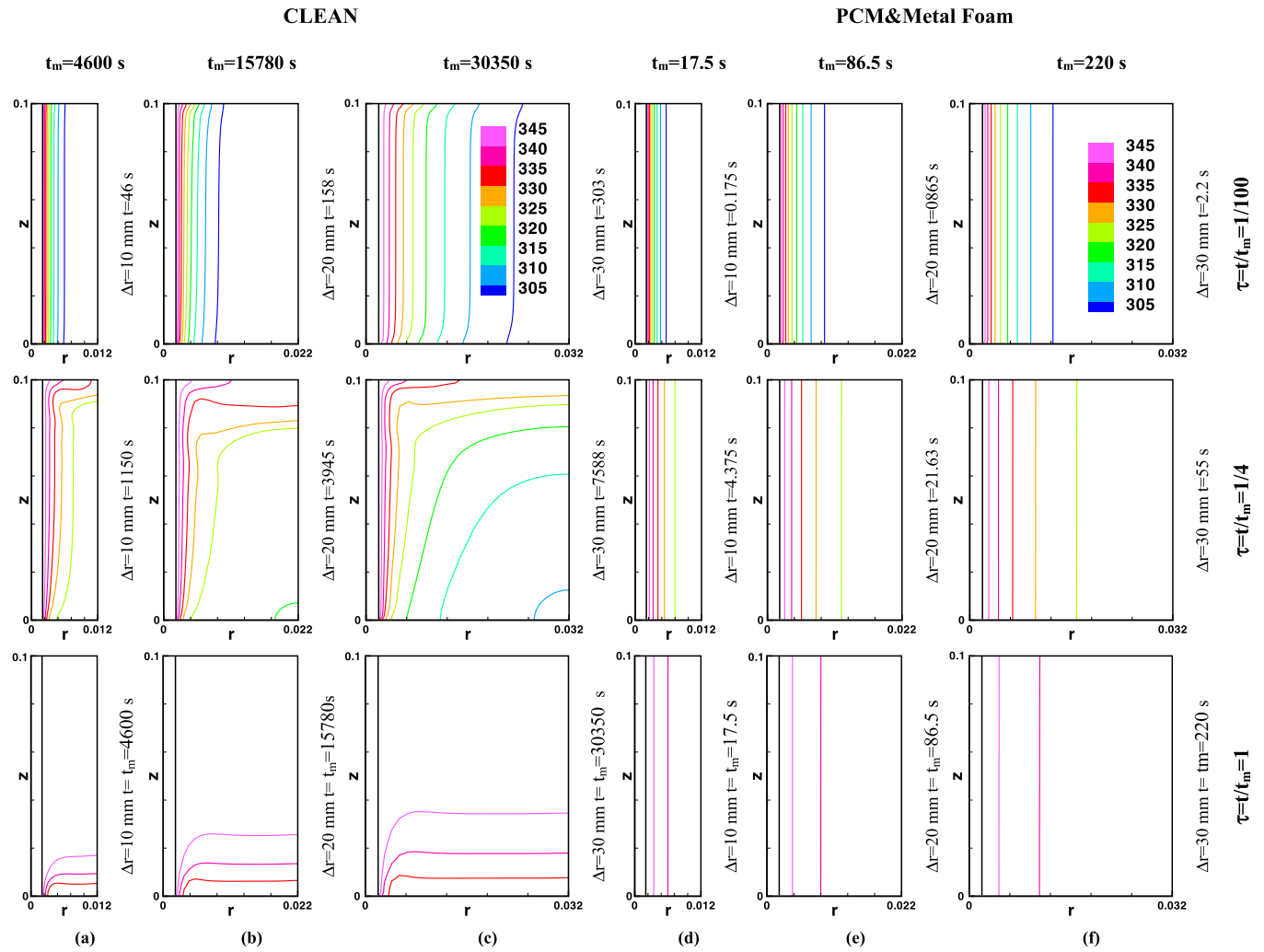

Fig. 8. Temperature fields for CLEAN and PCM with metal foam, three radius differences, Δr = 10, 20 and 30 mm and three different time as fraction of melting time τ = t/tm.

5. Conclusions

A numerical investigation and a scale analysis of the behaviors of latent heat thermal energy storage (LHTES) systems with phase change material (PCM) embedded in an aluminum foam were carried out. The storage was between two vertical coaxial cylinders. The enthalpy-porosity method to model the phase change process was employed and the Darcy-Forchheimer law and local thermal equilibrium model were assumed for the metal foam (aluminum foam). The results are shown in terms of liquid fraction, temperature fields, and stream-function fields as a function of time for the cases with and without the metal foam. The effect of porosity was also evaluated for the case with metal foam. The order of magnitude between the PCM-porous medium local temperature difference, and the global temperature difference, were estimated by means of the scale analysis. It is shown that the difference in local temperature in relation to the global temperature difference is less the greater the number of pores per inch (PPI). In fact, for PPI = 20, the local temperature difference with respect to the global temperature difference is 10^{-4} of order of magnitude, and the local thermal equilibrium assumption is satisfactory. Furthermore, the scale analysis results in terms of times and geometrical shapes related to the melting process, are satisfactorily confirmed by numerical results.

Increase in porosity increases the melting time because of an effective thermal conduction decrease of the whole system. The presence of metal foam significantly improved the heat transfer in the LHTES system, giving a much faster phase change process with respect to pure PCM, due to the dominant conduction phenomenon during the PCM melting. The differences between the pure PCM case and the PCM in metal foam with lower porosity shows that the melting time is about 4600 s, and about 20 s, respectively, with a difference of a two order of magnitude for the lowest volume of thermal storage here considered and about 30,000 s and 220 s, for the greatest volume under consideration. It is crucial to note that the ratio between the melting time for the CLEAN case, and for PCM and foam with lowest porosity decreases as the volume for assigned height increases, due to the high natural convection effect.

Liquid fraction and temperature fields helped to detect the presence of natural convection regime in pure PCM cases, whereas a complete diffusive phenomenon was observed for the cases with metal foam. This was confirmed by the stream function field. The different melting regimes were also in tandem with the scale analysis results.

The results enable us to understand how to provide the appropriate size of a storage system by means of the performance parameter “q”, in order to obtain the guidelines to choose a storage system with metal foam for a specific application, such as a solar energy system.

A lower volume with 80% of total volume in the CLEAN case presented a longer melting time for lower height and equal external cylinder base area, and a shorter melting time for lower base area and same height with respect to the CLEAN case.

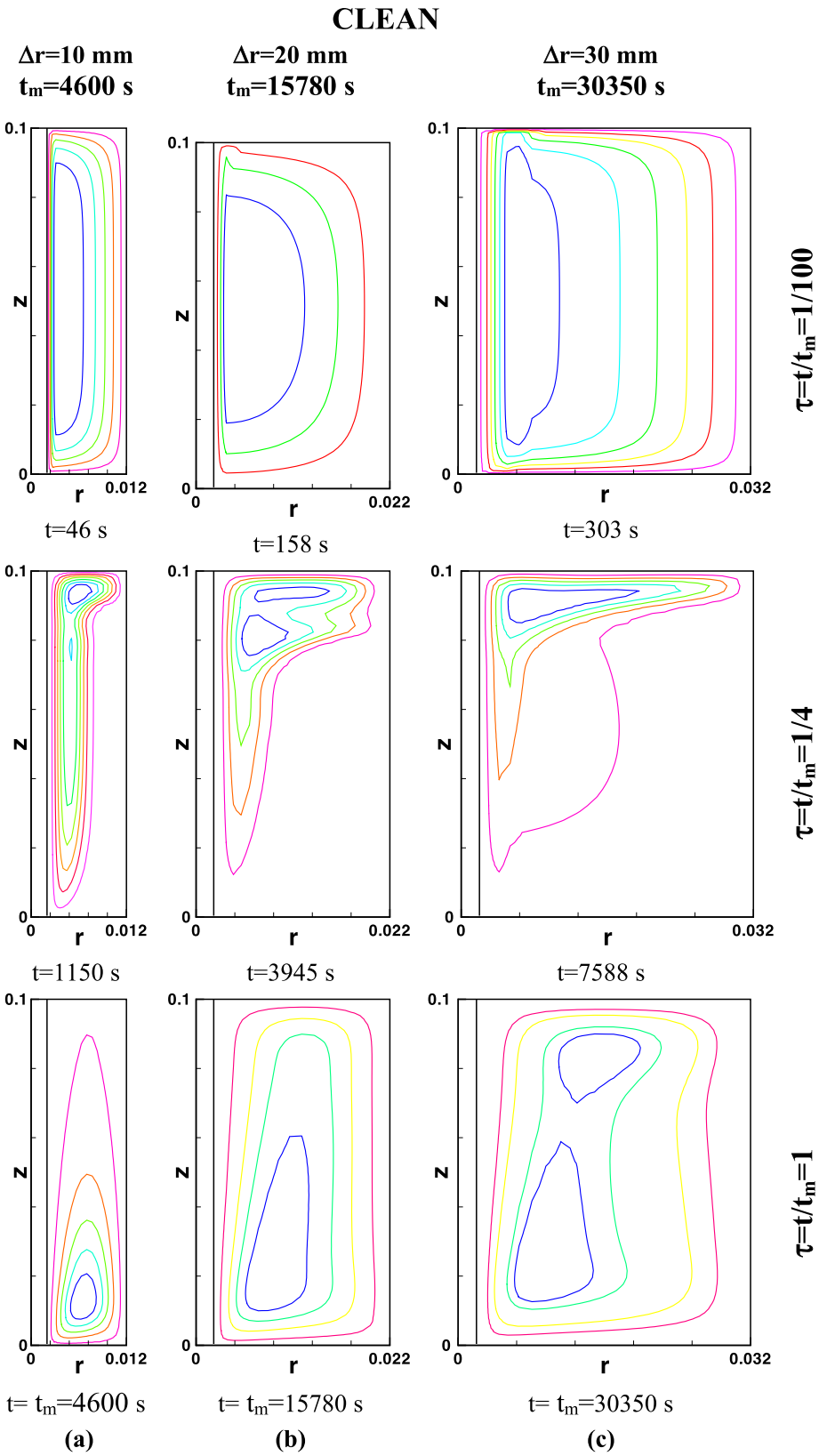

Fig. 9. Stream Function fields for CLEAN cases with three radius differences, Δr = 10, 20 and 30 mm and three different time as fraction of melting time $\tau = t/t_m$.

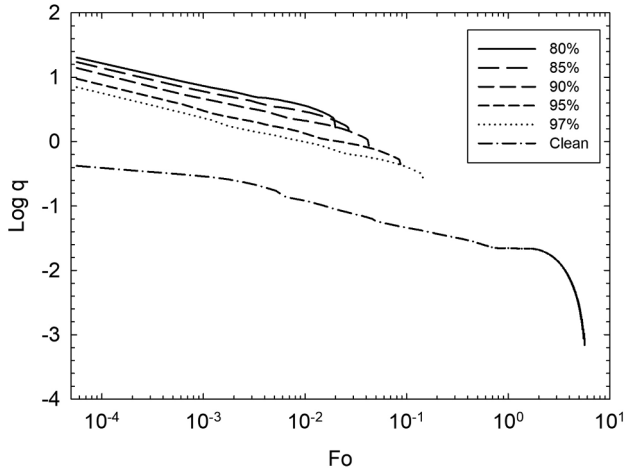

Fig. 10. Thermal performance parameter q as function of time for: CLEAN case and PCM in aluminum foam for different porosity values (0.80–0.97) and 20 PPI.

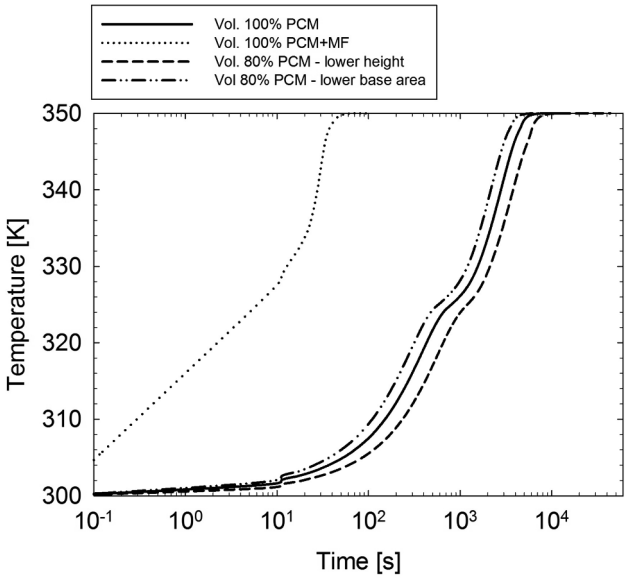

Fig. 11. Average temperature profile as a function of time for reduced volume, Vol. 80% PCM – lower height case and Vol 80% PCM – lower base area, CLEAN case volume, volume 100% PCM, and case with PCM in aluminum foam with $\varepsilon = 0.8$, volume 100% PCM + AF.

Declaration of Competing Interest

Author declares that there is no conflict of interest.

Appendix A. Supplementary material

Supplementary data to this article can be found online at https://doi.org/10.1016/j.applthermaleng.2019.113980.

References

[1] A. Gil, M. Medrano, I. Martorell, A. Lazaro, P. Dolado, B. Zalba, L.F. Cabeza, State of the art on high temperature thermal energy storage for power generation. Part 1 – concepts, materials and modellization, Renew. Sustain. Energy Rev. 14 (2010) 31–55, https://doi.org/10.1016/j.rser.2009.07.035.

[2] Y. Tian, C.Y. Zhao, A review of solar collectors and thermal energy storage in solar thermal applications, Appl. Energy 104 (2013) 538–553, https://doi.org/10.1016/j.apenergy.2012.11.051.

[3] S. Sabihuddin, A.E. Kiprakis, M. Mueller, A numerical and graphical review of energy storage technologies, Energies 8 (2015) 172–216, https://doi.org/10.3390/en8010172.

[4] L.F. Cabeza, Advances in Thermal Energy Storage Systems: Methods and Applications, Woodhead Publishing Series in Energy, Sawston, Cambridge, UK, 2014.

[5] I. Dincer, M. Rosen, Thermal Energy Storage: System and Application, 2nd ed., John Wiley & Sons, New York, 2010.

[6] G. Beckmann, P. V. Gilli, Thermal Energy Storage: Basics, Design, Applications to Power Generation and Heat Supply, Springer, Vienna, 2002.

[7] H. O. Paksoy, Thermal Energy Storage for Sustainable Energy Consumption: Fundamentals, Case Studies and Design, Springer, Berlin, 2007.

[8] S. Kalaiselvam, R. Parameshwaran, Thermal Energy Storage Technologies for Sustainability: Systems Design, Assessment and Applications, 1st ed., Academic Press, 2014.

[9] R. Dell, D. Rand, Energy storage a key technology for global energy sustainability, J. Power Sources 100 (2001) 2–17, https://doi.org/10.1016/S0378-7753(01)00894-1.

[10] A. Arteconi, N.J. Hewitt, F. Polonara, State of the art of thermal storage for demand-side management, Appl. Energy 93 (2012) 371–389, https://doi.org/10.1016/j.apenergy.2011.12.045.

[11] E. Oró, A. Gil, A. de Gracia, D. Boer, L.F. Cabeza, Comparative life cycle assessment of thermal energy storage systems for solar power plants, Renew. Energy 44 (2012) 166–173, https://doi.org/10.1016/j.renene.2012.01.008.

[12] J. Shao, J. Darkwa, G. Kokogiannakis, Review of phase change emulsions (PCMEs) and their applications in HVAC systems, Energy Build. 94 (2015) 200–217, https://doi.org/10.1016/j.enbuild.2015.03.003.

[13] J. Heier, C. Bales, V. Martin, Combining thermal energy storage with buildings – a review, Renew. Sustain. Energy Rev. 42 (2015) 1305–1325, https://doi.org/10.1016/j.rser.2014.11.031.

[14] S. Pintaldi, C. Perfumo, S. Sethuvenkatraman, S. White, G. Rosengarten, A review of thermal energy storage technologies and control approaches for solar cooling, Renew. Sustain. Energy Rev. 41 (2015) 975–995, https://doi.org/10.1016/j.rser.2014.08.062.

[15] A. Hesaraki, S. Holmberg, F. Haghighat, Seasonal thermal energy storage with heat pumps and low temperatures in building projects – a comparative review, Renew. Sustain. Energy Rev. 43 (2015) 1199–1213, https://doi.org/10.1016/j.rser.2014.12.002.

[16] V.G. Gude, Energy storage for desalination processes powered by renewable energy and waste heat sources, Appl. Energy 137 (2015) 877–898, https://doi.org/10.1016/j.apenergy.2014.06.061.

[17] Y. Fulpagare, A. Bhargav, Advances in data center thermal management, Renew. Sustain. Energy Rev. 43 (2015) 981–996, https://doi.org/10.1016/j.rser.2014.11.056.

[18] R.K. Sharma, P. Ganesan, V.V. Tyagi, H.S.C. Metselaar, S.C. Sandaran, Developments in organic solid-liquid phase change materials and their applications in thermal energy storage, Energy Convers. Manage. 95 (2015) 193–228, https://doi.org/10.1016/j.enconman.2015.01.084.

[19] L.F. Cabeza, A. Gutierrez, C. Barreneche, S. Ushak, A.G. Fernández, A. Inés Fernádez, M. Grágeda, Lithium in thermal energy storage: a state-of-the-art review, Renew. Sustain. Energy Rev. 42 (2015) 1106–1112, https://doi.org/10.1016/j.rser.2014.10.096.

[20] T. Yan, R.Z. Wang, T.X. Li, L.W. Wang, I.T. Fred, A review of promising candidate reactions for chemical heat storage, Renew. Sustain. Energy Rev. 43 (2015) 13–31, https://doi.org/10.1016/j.rser.2014.11.015.

[21] M. Koschenz, B. Lehmann, Development of a thermally activated ceiling panel with PCM for application in lightweight and retrofitted buildings, Energy Build. 36 (6) (2004) 567–578, https://doi.org/10.1016/j.enbuild.2004.01.029.

[22] I.M. Bugaje, Enhancing the thermal response of latent heat storage systems, Int. J. Energy Res. 21 (1997) 759–766.

[23] K. Boomsma, D. Poulikakos, F. Zwick, Metal foams as compact high performance heat exchangers, Mech. Mater. 35 (2003) 1161–1176, https://doi.org/10.1016/j.mechmat.2003.02.001.

[24] A. Sari, C. Alkan, A. Karaipekli, O. Uzun, Microencapsulated n-octacosane as phase change material for thermal energy storage, Sol. Energy 83 (2009) 1757–1763, https://doi.org/10.1016/j.solener.2009.05.008.

[25] J. Fukai, Y. Hamada, Y. Morozumi, O. Miyatake, Improvement of thermal characteristics of latent heat thermal energy storage units using carbon-fiber brushes: experiments and modeling, Int. J. Heat Mass Transf. 46 (2003) 4513–4525, https://doi.org/10.1016/S0017-9310(03)00290-4.

[26] X. Py, R. Olives, S. Mauran, Paraffin/Porous graphite-matrix composite as a high and constant power thermal storage material, Int. J. Heat Mass Transf. 44 (2001) 2727–2737, https://doi.org/10.1016/S0017-9310(00)00309-4.

[27] L.C. Chow, J.K. Zhoong, J.E. Beam, Thermal conductivity enhancement for phase change storage media, Int. Commun. Heat Mass Transf. 83 (1996) 1757–1763, https://doi.org/10.1016/0735-1933(95)00087-9.

[28] C. Y. Zhao, D. Zhou, Z. G. Wu, Heat transfer enhancement of phase change materials (PCMs) in low and high temperature thermal storage by using porous materials, Proceedings of 14th International Heat Transfer Conference IHTC 14th, vol. 7, pp. 435–441, Whashington, DC, USA, 2010.

[29] Y. Tian, C. Y. Zhao, Thermal analysis in phase change materials (PCMs) embedded with metal foams, Proceedings of 14th International Heat Transfer Conference IHTC 14th, vol. 7, pp. 425–434, Whashington, DC, USA, 2010.

[30] C.Y. Zhao, W. Lu, Y. Tian, Heat transfer enhancement for thermal energy storage using metal foams embedded within phase change materials (PCMs), Sol. Energy 84 (2010) 1402–1412, https://doi.org/10.1016/j.solener.2010.04.022.

[31] Y. Tian, C.Y. Zhao, Heat transfer analysis for phase change materials (PCMs), Proceedings of 11th International Conference on Energy Storage, Effstock,

Stockholm, (2009).
[32] A. Siahpush, J. O'Brien, J. Crepeau, Phase change heat transfer enhancement using copper porous foam, ASME J. Heat Transf. 130 (2008) 082301, https://doi.org/10.1115/1.2928010.
[33] D. Zhou, C.Y. Zhao, Experimental investigations on heat transfer in phase change materials (PCMs) embedded in porous materials, Appl. Therm. Eng. 31 (2011) 970–977, https://doi.org/10.1016/j.applthermaleng.2010.11.022.
[34] Z. Chen, D. Gao, J. Shi, Experimental and numerical study on melting of phase change materials in metal foams at pore scale, Int. J. Heat Mass Transf. 72 (2014) 646–655, https://doi.org/10.1016/j.ijheatmasstransfer.2014.01.003.
[35] K. Nithyanandam, R. Pitchumani, Computational studies on metal foam and heat pipe enhanced latent thermal energy storage, ASME J. Heat Transf. 136 (2014) 051503, https://doi.org/10.1115/1.4026040.
[36] S.S. Sundarram, W. Li, The effect of pore size and porosity on thermal management performance of phase change material infiltrated microcellular metal foams, Appl. Therm. Eng. 64 (2014) 147–154, https://doi.org/10.1016/j.applthermaleng.2013.11.072.
[37] Z. Liu, Y. Yao, H. Wu, Numerical modeling for solid–liquid phase change phenomena in porous media: shell-and-tube type latent heat thermal energy storage, Appl. Energy 112 (2013) 1222–1232, https://doi.org/10.1016/j.apenergy.2013.02.022.
[38] Y.B. Tao, Y. You, Y.L. He, Lattice Boltzmann simulation on phase change heat transfer in metal foams/paraffin composite phase change material, Appl. Therm. Eng. 93 (2016) 476–485, https://doi.org/10.1016/j.applthermaleng.2015.10.016.
[39] P. Zhang, Z. Meng, H. Zhu, Y. Wang, S. Peng, Experimental and numerical study of heat transfer characteristics of a paraffin/metal foam composite PCM, Energy Procedia 75 (2015) 3091–3097, https://doi.org/10.1016/j.egypro.2015.07.637.
[40] J. Yang, L. Yang, C. Xu, X. Du, Numerical analysis on thermal behavior of solid-liquid phase change within copper foam with varying porosity, Int. J. Heat Mass Transf. 84 (2015) 1008–1018, https://doi.org/10.1016/j.ijheatmasstransfer.2015.01.088.
[41] A. Atal, Y. Wang, M. Harsha, S. Sengupta, Effect of porosity of conducting matrix on a phase change energy storage device, Int. J. Heat Mass Transf. 93 (2016) 9–16, https://doi.org/10.1016/j.ijheatmasstransfer.2015.09.033.
[42] O. Mesalhy, K. Lafdi, A. Elgafy, K. Bowman, Numerical study for enhancing the thermal conductivity of phase change material (PCM) storage using high thermal conductivity porous matrix, Energy Convers. Manage. 46 (2005) 847–867, https://doi.org/10.1016/j.enconman.2004.06.010.
[43] A. Kumar, S.K. Saha, Energy and exergy analyses of medium temperature latent heat thermal storage with high porosity metal matrix, Appl. Therm. Eng. 109 (2016) 911–923, https://doi.org/10.1016/j.applthermaleng.2016.04.161.
[44] A. Kumar, S.K. Saha, Latent heat thermal storage with variable porosity metal matrix: a numerical study, Renew. Energy 125 (2018) 962–973, https://doi.org/10.1016/j.renene.2018.03.030.
[45] J. Yang, L. Yang, C. Xu, X. Du, Experimental study on enhancement of thermal energy storage with phase-change material, Appl. Energy 169 (2016) 164–176, https://doi.org/10.1016/j.apenergy.2016.02.028.
[46] C. Wang, T. Lin, N. Li, H. Zheng, Heat transfer enhancement of phase change composite material: copper foam/paraffin, Renew. Energy 96 (2016) 960–965, https://doi.org/10.1016/j.renene.2016.04.039.
[47] X. Huang, Y. Lin, G. Alva, G. Fang, Thermal properties and thermal conductivity enhancement of composite phase change materials using myristyl alcohol/metal foam for solar thermal storage, Sol. Energy Mater. Sol. Cells 170 (2017) 68–76, https://doi.org/10.1016/j.solmat.2017.05.059.
[48] Z. Zhang, J. Cheng, X. He, Numerical simulation of flow and heat transfer in composite PCM on the basis of two different models of open-cell metal foam skeletons, Int. J. Heat Mass Transf. 112 (2017) 959–971, https://doi.org/10.1016/j.ijheatmasstransfer.2017.05.012.
[49] F. Zhu, C. Zhang, X. Gong, Numerical analysis on the energy storage efficiency of phase change material embedded in finned metal foam with graded porosity, Appl. Therm. Eng. 123 (2017) 256–265, https://doi.org/10.1016/j.applthermaleng.2017.05.075.
[50] Z. Zhang, X. He, Three-dimensional numerical study on solid-liquid phase change within open-celled aluminum foam with porosity gradient, Appl. Therm. Eng. 113 (2017) 298–308, https://doi.org/10.1016/j.applthermaleng.2016.10.173.
[51] P. Zhang, Z.N. Meng, H. Zhu, Y.L. Wang, S.P. Peng, Melting heat transfer characteristics of a composite phase change material fabricated by paraffin and metal foam, Appl. Energy 185 (2017) 1971–1983, https://doi.org/10.1016/j.apenergy.2015.10.075.
[52] Z. Zhu, Y. Huang, N. Hua, Y. Zeng, L. Fan, Transient performance of a PCM-based heat sink with a partially filled metal foam: effects of the filling height ratio, Appl. Therm. Eng. 128 (2018) 966–972, https://doi.org/10.1016/j.applthermaleng.2017.09.047.
[53] J. Yang, X. Du, L. Yang, Y. Yang, Numerical analysis on the thermal behavior of high temperature latent heat thermal energy storage system, Sol. Energy 98 (2013) 543–552, https://doi.org/10.1016/j.solener.2013.10.028.
[54] S. Krishnan, J.Y. Murthy, S.V. Garimella, A two-temperature model for solid–liquid phase change in metal foams, ASME J. Heat Transf. 127 (2005) 995–1004, https://doi.org/10.1115/1.2010494.
[55] B. Buonomo, D. Ercole, O. Manca, S. Nardini, Numerical investigation on thermal behaviors of two-dimensional latent thermal energy storage with PCM and aluminum foam, J. Phys.: Conf. Series 796 (2017) 012031, https://doi.org/10.1088/1742-6596/796/1/012031.
[56] B.D. Buonomo, O. Ercole, S. Manca, Nardini Numerical investigation on Nano-PCM in aluminum foam in latent thermal energy storages, paper no 56, , 3rd AIGE/IIETA International Conference and 12th AIGE 2018 Conference, Reggio Calabria – Messina, (2018).
[57] F. Agyenim, N. Hewitt, P. Eames, M. Smyth, A review of materials, heat transfer and phase change problem formulation for latent heat thermal energy storage systems (LHTESS), Renew. Sustain. Energy Rev. 14 (2) (2010) 615–628, https://doi.org/10.1016/j.rser.2009.10.015.
[58] V.R. Voller, C. Prakash, A fixed grid numerical modelling methodology for convection-diffusion mushy region phase-change problems, Int. J. Heat Mass Transf. 30 (1987) 1709–1719, https://doi.org/10.1016/0017-9310(87)90317-6.
[59] V.V. Calmidi, R.L. Mahajan, Forced convection in high porosity metal foams, ASME J. Heat Transf. 122 (2000) 557–565, https://doi.org/10.1115/1.1287793.
[60] Rubitherm GmBH, www.rubitherm.de.
[61] Ansys Incorporated, Fluent User Manual, 2014.
[62] S.H. Tasnim, R. Hossain, S. Mahmud, A. Dutta, Convection effect on the melting process of nano-PCM inside porous enclosure, Int. J. Heat Mass Transf. 85 (2015) 206–220.
[63] P. Jany, A. Bejan, Scaling theory of melting with natural convection in an enclosure, Int. J. Heat Mass Transfer 31 (6) (1988) 1221–1235, https://doi.org/10.1016/0017-9310(88)90065-8.
[64] A. Bejan, Convection Heat Transfer, 4th ed., Wiley, Hoboken, 2013.
[65] S. Lorente, A. Bejan, J.L. Niu, Phase change heat storage in an enclosure with vertical pipe in the center, Int. J. Heat Mass Transf. 72 (2014) 329–335, https://doi.org/10.1016/j.ijheatmasstransfer.2014.01.021.